Computational Mechanics
https://doi.org/10.1007/s00466-023-02424-6

ORIGINAL PAPER

Microstructurally-informed stochastic inhomogeneity of material properties and material symmetries in 3D-printed 316 L stainless steel

Shanshan Chu[1] · Athanasios Iliopoulos[2] · John Michopoulos[2] · Andrew Birnbaum[2] · John Steuben[2] · Colin Stewart[3] · Patrick Callahan[3] · David Rowenhorst[3] · Johann Guilleminot[1]

Received: 28 June 2023 / Accepted: 14 November 2023

Abstract
Stochastic mesoscale inhomogeneity of material properties and material symmetries are investigated in a 3D-printed material. The analysis involves a spatially-dependent characterization of the microstructure in 316 L stainless steel, obtained through electron backscatter diffraction imaging. These data are subsequently fed into a Voigt–Reuss–Hill homogenization approximation to produce maps of elasticity tensor coefficients along the path of experimental probing. Information-theoretic stochastic models corresponding to this stiffness random field are then introduced. The case of orthotropic fields is first defined as a high-fidelity model, the realizations of which are consistent with the elasticity maps. To investigate the role of material symmetries, an isotropic approximation is next introduced through ad-hoc projections (using various metrics). Both stochastic representations are identified using the dataset. In particular, the correlation length along the characterization path is identified using a maximum likelihood estimator. Uncertainty propagation is finally performed on a complex geometry, using a Monte Carlo analysis. It is shown that mechanical predictions in the linear elastic regime are mostly sensitive to material symmetry but weakly depend on the spatial correlation length in the considered propagation scenario.

Keywords Additive manufacturing · Material symmetry · Random field · Stochastic modeling · Uncertainty quantification

1 Introduction

Additive manufacturing, commonly known as 3D printing, has revolutionized materials engineering by enabling the fabrication of intricate geometries in multiple length scales with unparalleled design and customization options. Among the wide range of materials used in additive manufacturing, 316 L stainless steel has garnered significant attention due to its excellent mechanical properties, high corrosion resistance, and suitability for diverse applications, including aerospace, automotive, and medical implants (see [1–3] for example).

In practice, extensive experimental evidence gathered using, scanning electron microscopy (SEM), X-ray diffraction (XRD), and electron backscatter diffraction (EBSD) imaging, shows that the microstructure of 3D-printed 316 L stainless steel can exhibit stronger stochastic inhomogeneity (in the form of spatial variations in microstructural features, such as grain size, grain orientation, and other microscale characteristics) and nonstationary effects than forged, rolled, or extruded steel [4–7]. These features are the net result of complex, multiphysics processing conditions where local cooling rate, solidification behavior, and thermal history vary as the material is being deposited [8–10]. Such microstructural inhomogeneity can result, in turn, in uncertainties in constitutive modeling, whether it be on the elastic regime, tensile strength, hardness, or fatigue performance. These fluctuations affect the overall performance of the printed parts [11–15] and often lead to over-conservative design procedures. Understanding and characterizing these stochastic variations is therefore an essential step toward the prediction of printed parts performance and optimization of additive manufacturing processes [16].

B Johann Guilleminot
johann.guilleminot@duke.edu

1 Department of Civil and Environmental Engineering, Duke University, Durham, NC 27708, USA

2 Computational Multiphysics Systems Laboratory, Center of Computational Material Science, Naval Research Laboratory, Washington, DC 20375, USA

3 Metallurgical Alloy Design Section, Multifunctional Materials Branch, Naval Research Laboratory, Washington, DC 20375, USA

Published online: 16 December 2023

In recent years, there has been growing interest in developing modeling approaches to characterize and predict the mechanical properties of additive manufactured parts based on fine-scale descriptors. Machine learning techniques and in particular, deep learning (e.g., neural-network-based) methods have emerged as powerful tools for approximating the usually high-dimensional, nonlinear relationship between the selected microstructural features and mechanical properties of interest [17–19]. These approaches, however, typically require large datasets to be trained with reasonable accuracy (note that a discussion about such techniques, and methods to accelerate convergence in training, is outside the scope of this work). In addition, potential non-stationary effects can pose challenges in developing predictive models, as the variability in probabilistic properties across different regions of the printed parts adds another layer of complexity in terms of experimental characterization and statistical processing.

Many other studies have attempted to investigate microstructure randomness and defects in 3D-printed metals, and their impact in the mechanical response at the macroscale; see [20–26] to list a few. Such approaches usually rely on very local experimental information given the cost and complexity of reliably acquiring microscopy- or diffusion-based measurements over an entire structure. Some papers reported on the characterization and propagation of nonstationary effects over restricted domains; see, e.g., [27, 28]. As an alternative to such methodologies where data, obtained at a fine scale, are plugged into models that are built at a coarser scale, other frameworks were proposed where data and models are considered at coarse (e.g., structural) and fine (e.g., mesoscopic) scales, respectively; see [29].

The aim of this work is to specifically investigate stochastic inhomogeneity and the role of material symmetries in 3D-printed 316L stainless steel, by combining *location-dependent* EBSD characterization on a geometry processed by power bed fusion, multiscale analysis, and stochastic modeling for uncertainty quantification. Once fully calibrated and validated using an ad hoc statistical technique (depending on the amount and nature of available data), under a given validation scenario and for a specific quantity of interest (see, e.g., [30]), the proposed stochastic model can used to sample the elasticity field and predict, through uncertainty propagation (using an appropriate stochastic solver; see [30, 31] for reviews), the stochastic mechanical properties of the part. Our contributions are as follows:

- By combining EBSD results with an upscaling approach, we first obtain a map of elasticity parameters as a function of location, hence enabling a random field analysis along the characterization path.
- We then derive a probabilistic model for elasticity random fields with values in the set of orthotropic tensors (defined in the reference frame), and identify its first-order marginal probability distribution.
- We further define an isotropic approximation to the above orthotropic field, and similarly identify its first-order marginal probability distribution.
- We propose a methodology, based on the maximum likelihood method, to identify one correlation length of the random fields, using one experimental sample.
- Using the above results, we perform uncertainty propagation to study the impact of the material symmetry and correlation structure on the structural response.

The rest of this paper is organized as follows. Material processing and experimental characterization are first presented in Sect. 2. In particular, we discuss the identification of elasticity maps on the printed geometry and investigate the construction of an isotropic surrogate model. The stochastic modeling approach is then introduced in Sect. 3. An overview of the framework is provided, and explicit results are given for classes of isotropic and orthotropic elasticity random fields. Model calibration is subsequently addressed in Sect. 4, using both real samples and their isotropic approximations. Section 5 is devoted to uncertainty propagation where the influence of material symmetry is specifically studied. Concluding remarks are finally provided in Sect. 6.

2 Additive manufacturing processing and multiscale analysis

2.1 Material processing

In order to quantify spatial inhomogeneity and anisotropy, an L-shaped Conformal Pressure Vessel (CPV) was designed and manufactured (as shown in Fig. 1a) out of SS-316L alloy powder, using a General Electric Concept Laser M2 Laser Powder Bed Fusion (LPBF) system. The utilized processing parameters were the nominal ones, defined by the manufacturer as follows: laser power 370 [W], Gaussian beam spot size 160 [μm] and velocity of 900 [mm/s]. The time between the end of a layer (in $x-y$ plane) and the beginning of the next was 12 seconds approximately. Layer deposition direction was along the z axis. Let $\boldsymbol{x} = (x, y, z)^T$ be a point in the Cartesian coordinate system (representing the laboratory frame of reference) shown in Fig. 1. It should be noted that the effects of the printing parameters, such as scan spacing and timelapse, on the crystallization process and on the stochastic parameters of the microstructure were not explored as they fall outside the scope and goals of the present effort. However, a significant corpus of prior work is specifically devoted to this topic as in [12, 32]. The CPV was sectioned along vertical and horizontal lines (as depicted by the black lines in Fig. 1a) to verify that the microstructure of the one closest

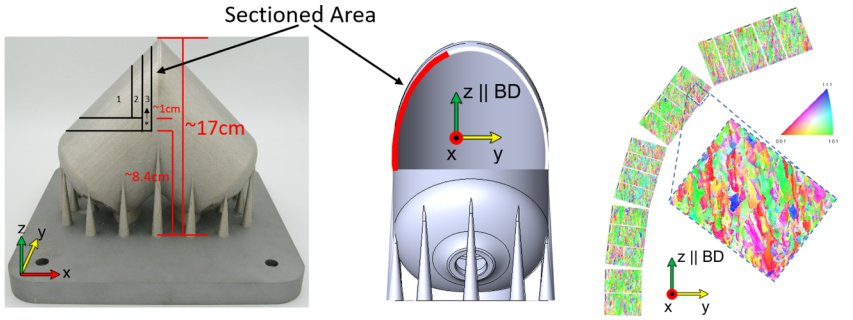

Fig. 1 The designed and manufactured CPV: as-built part, with global frame (O, x, y, z), and CAD model (left). The red line in the CAD model indicates the curve along which samples are collected for microstructural characterization (from [33])

(b) Inverse pole figure maps along the curvilinear path. Color indicates crystal direction along the build direction.

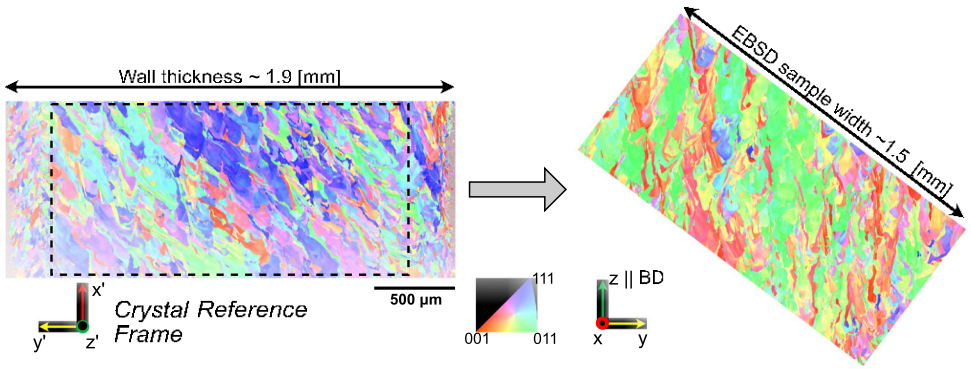

Fig. 2 Inverse pole figure (IPF) maps of one of the CPV segment cross-sections. Left: Original scan showing the entire thickness of the CPV wall, along with the as-collected crystal reference frame. Right: outline cropped IPF map along with the rotated crystal reference frame that now aligns with the global frame (O, x, y, z)

to the CPV center mirror-plane (offset by 0.5 [cm], shown with a red line) in Fig. 1a is statistically equivalent with the microstructure from the previous rest of the sections. The red line section in Fig. 1a was selected because it provides the largest range of the build direction and of the CPV and therefore provides the best choice for determining the variability of the microstructure as a function of the build direction. The thickness of the wall at this location is 1.9 [mm]. The resulting exposed surface was polished with a final polishing step using 0.05 [μm] colloidal silica, to prepare it for Electron Back-scattering Diffraction (EBSD) data collection.

A total of 18 segments were prepared along the exposed surface created by the previously produced sectioning and were used for collecting the associated EBSD data. The number of segments extracted from this section was selected based on finding an area that had a relatively constant overhang angle, but also enough grains to provide a reasonable estimate of the local orientation texture (on the order of 100–300 grains). The EBSD characterization was performed to quantify the spatial evolution of microstructural features and crystallographic texture; see Fig. 1b. The EBSD data was collected on a Tescan Mira 3 field emission scanning electron microscope, using an EDAX Velocity Super EBSD detector. Each scan measured approximately 1.5 [mm] × 0.9 [mm] on average with a 1 [μm] step size, with each point measuring the crystal phase (here only FCC was detected) and the crystal orientation relative to a crystal reference frame aligned to the EBSD scan. The EBSD scans were taken at increasing angles along the curved part (Fig. 1b). Therefore, the crystal reference frame of each EBSD map for each segment was rotated so that they were all coincident with the CAD coordinate system as illustrated in Fig. 2. In general, it was observed that lower on the piece, where the wall is mostly vertical along the z-direction, there appears to be significant texture with the 011 crystal direction aligned with the build direction, as indicated by the large number of green areas in the inverse pole figure (IPF) maps Fig. 1b, which indicate crystal direction parallel with the build direction. However, further up the part where the piece starts becoming more horizontal along the Y direction, more 001 grains aligned with the build direction are observed, with the IPF maps showing an increase in the number of red grains in the IPF.

The assessment of such spatial variability is key to random field modeling, as additive manufacturing is known to produce microstructures that substantially differ from the ones obtained through standard manufacturing techniques as depicted in Fig. 2. In particular, complex variations in grain size and shape are observed and defects (e.g., porosity) can be created over a wide range of scales. Grain morphology and texture can be maintained or varied across resolidification fronts as well. All of these features often result in significant anisotropy and inhomogeneity, depending on the scale of

analysis, which in turn impact the mechanical properties and behavior of the structure. Notice that this characterization is pretty unique in the literature, where multiscale settings (see, e.g., [20–23]) are generally deployed on digitally synthesized microstructures or microstructures that are experimentally characterized at one single location, thus potentially missing anisotropies caused by the varying processing conditions within the part. Finally, it is noted that although the maps are 2D, EBSD enables the calculation of the 3D crystallographic orientation via the characterization of all three Euler angles, i.e. the orientation of the respective crystal with respect to the global sample frame. It should also be noted that the horizontal thermal history controlling the microstructure evolves within the thin shell wall of the CPV the same way in both of the two horizontal orthogonal directions and varies significantly only in the build directions that imposes the strongest thermal history. However, this argument based on the similarity of the thermal history should be verified in a future effort by examining the microstructure along the azimuthal line cuts of the CPV.

2.2 Analysis of elasticity maps

The single crystal exhibits a face-centered cubic (FCC) symmetry and is defined by a fourth-order elasticity tensor, denoted by C^{xtal} (with associated compliance tensor $S^{\text{xtal}} = C^{\text{xtal}-1}$). Let $[C^{\text{xtal}}]$ be the Voigt representation of C^{xtal}, given in its reference frame by

$$[C^{\text{xtal}}] = \begin{bmatrix} a_{11} & a_{12} & a_{12} & 0 & 0 & 0 \\ & a_{11} & a_{12} & 0 & 0 & 0 \\ & & a_{11} & 0 & 0 & 0 \\ & & & a_{44} & 0 & 0 \\ & \text{Sym.} & & & a_{44} & 0 \\ & & & & & a_{44} \end{bmatrix}, \tag{1}$$

where $a_{11} = 236$, $a_{12} = 134$ and $a_{44} = 111$ [GPa] (see [34]). The indices of the matrix are related to the coordinate system of Fig. 1a according to:

$$\begin{matrix} 11 \\ 22 \\ 33 \\ 12, 21 \\ 23, 32 \\ 13, 31 \end{matrix} \leftrightarrow \begin{matrix} 1 \\ 2 \\ 3 \\ 4 \\ 5 \\ 6 \end{matrix} \leftrightarrow \begin{matrix} x \\ y \\ z \\ xy \\ yz \\ xz \end{matrix}. \tag{2}$$

In order to generate elasticity maps $\{z \to C^{\text{hom}}_{ijk}(z)\}_{i,j,k,}$, the Voigt–Reuss–Hill average

$$C^{\text{hom}}(z) = \frac{1}{2}(C^V(z) + C^R(z)) \tag{3}$$

was estimated at the $N_p = 18$ sampled locations, where C^V and C^R are the so-called Voigt and Reuss bounds, respectively (see [35, 36] for a review). These bounds were computed, for each EBSD z, as

$C^V(z)$ with

$$C^V_{ijk}(z) = \frac{1}{N_g}\sum_{n=1}^{N_g} g^n_{ip}(z)^T g^n_{jq}(z)^T g^n_{kr}(z)^T g^n_s(z)^T C^{\text{xtal}}_{pqrs} \tag{4}$$

and

$C^R(z) = S^R(z)^{-1}$, with

$$S^R_{ijk}(z) = \frac{1}{N_g}\sum_{n=1}^{N_g} g^n(z)^T_{ip} g^n{}_q(z)^T_j g^n{}_r(z)^T_k g^n(z)^T_s S^{\text{xtal}}{}_{pqr}, \tag{5}$$

where $[g^n(z)]$ denotes the measured rotation tensor that relates the crystal reference frame (in the EBSD scan centered at location z, indexed by p, q, r, s) to the sample and therefore global reference frame (indexed by i, j, k, l), N_g is the number of data points in the EBSD scan, and n is the index of the data point. Each data point corresponds to a pixel in the EBSD scan. In the present analysis, it was assumed that slicing at different locations along the $x-z$ or $y-z$ planes would yield statistically equivalent crystallographic structures.

The homogenized elasticity tensor $[C^{\text{hom}}(z_1)]$ (in Voigt form and in the global coordinate system) at the first point with vertical coordinate $z_1 = 4.88$ [mm] is given by

$$[C^{\text{hom}}(z_1)] = \begin{bmatrix} 286.4 & 105.5 & 112.1 & 0 & 0 & 0 \\ & 282.6 & 115.9 & 0 & 0 & 0 \\ & & 276 & 0 & 0 & 0 \\ & & & 83.3 & 0 & 0 \\ & \text{Sym.} & & & 79.7 & 0 \\ & & & & & 73.8 \end{bmatrix} \tag{6}$$

for instance (in [GPa]). Maps of elasticity components as a function of the vertical coordinate z are shown in Figs. 3, 4 and 5. Non-negligible spatial variations are observed along the z-axis, and it is seen that the predicted homogenized tensors remain orthotropic regardless of the location—due to the symmetry exhibited by the crystal and to the transformation from the local to the global frame. It is also observed that these tensors, while orthotropic, may be approximated by isotropic tensors, with the goal of reducing the parameterization. In the next section, we introduce the isotropic approximation of the elasticity maps.

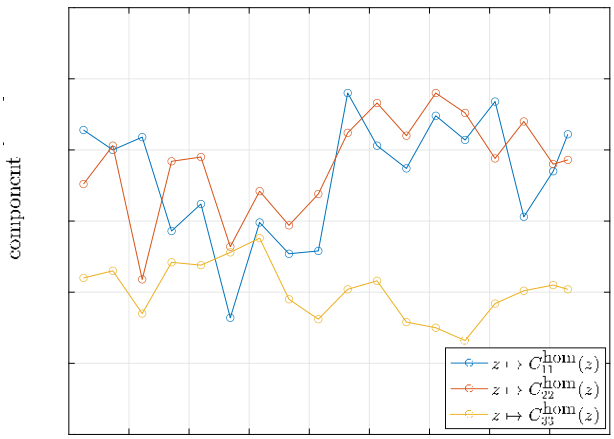

Fig. 3 Graphs of the elasticity maps $\{z \to C_{ij}^{\mathrm{hom}}(z)\}_{i,j}$, for $i = j \in \{1, 2, 3\}$

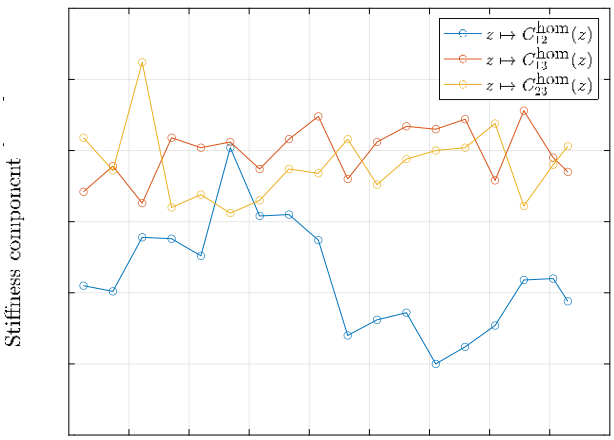

Fig. 4 Graphs of the elasticity maps $\{z \to C_{ij}^{\mathrm{hom}}(z)\}_{i,j}$, for $\{ij\} \in \{\{12\}, \{13\}, \{23\}\}$

2.3 Definition of an isotropic approximation

For any elasticity tensor $[C^{\mathrm{hom}}]$ (at a specific location), an isotropic approximation can be defined by the bulk and shear moduli k and μ given by

$$(k, \mu) = \operatorname{argmin}_{(k^{\mathbb{R}}, \mu^{\mathbb{R}}) \in \mathbb{R}^2_{>0}} d([C^{\mathrm{hom}}], [C_{\mathrm{iso}}^{\mathrm{hom}}(k^{\mathbb{R}}, \mu^{\mathbb{R}})]), \tag{7}$$

where d is an appropriate metric and $[C_{\mathrm{iso}}^{\mathrm{hom}}(k^{\mathbb{R}}, \mu^{\mathbb{R}})]$ is the isotropic elasticity tensor defined by bulk and shear moduli $k^{\mathbb{R}}$ and $\mu^{\mathbb{R}}$. Several metrics have been studied in the literature of theoretical elasticity (see, e.g., [37–39]), including the

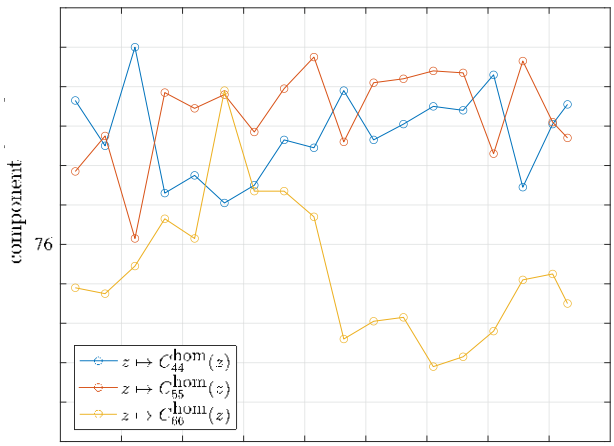

Fig. 5 Graphs of the elasticity maps $\{z \to C_{ij}^{\mathrm{hom}}(z)\}_{i,j}$, for $i = j \in \{4, 5, 6\}$

Euclidean, Log-Euclidean, and Riemannian metrics defined as

$$d([A], [B]) = \|[A] - [B]\|_F, \tag{8}$$

$$d([A], [B]) = \|\log([A]) - \log([B])\|_F, \tag{9}$$

$$d([A], [B]) = \|\log([A]^{-1/2}[B][A]^{-1/2})\|_F. \tag{10}$$

respectively. It should be noticed that the Log-Euclidean and Riemannian metrics are invariant under inversion, meaning that they produce the same (isotropic) approximation regardless of whether the problem is formulated in terms of the elasticity or compliance matrix. Solving the constrained optimization problem in Eq. (7) at all locations along the curvilinear coordinate s_3 then allows us to compute the associated realizations of the bulk and shear moduli, for the three above metrics. Implementation was verified by reproducing the results in [37, 39]. These realizations (one realization per elastic modulus) are shown in the two subpanels in Fig. 6. The graphs obtained for the Log-Euclidean and Riemannian metrics are visually indistinguishable given that the numerical results coincide up to seven digits. This proximity is consistent with results observed elsewhere; see [38] for a discussion. In addition, it is seen that the bulk modulus is less sensitive to the choice of the metric than the shear modulus—a qualitative result that was already reported in [39] (see Eq. (158) therein). These results will be used in Sect. 3 to discuss the relevance of the isotropic approximation in terms of variability prediction.

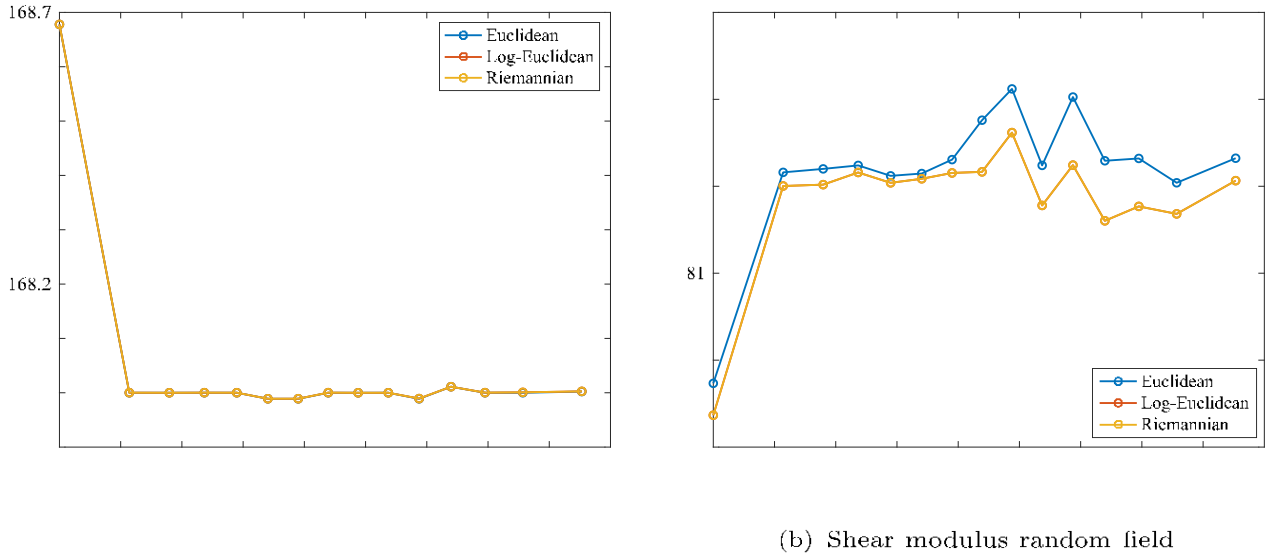

(b) Shear modulus random field

Fig. 6 Realization of the bulk and shear modulus random field, associated with the isotropic approximation, for the Euclidean, Log-Euclidean, and Riemannian metrics

3 Stochastic modeling

3.1 Overview of the stochastic modeling approach

We consider the stochastic modeling of the elasticity tensor random field written in Voigt form, denoted by $\{[\boldsymbol{C}(\boldsymbol{x})], \boldsymbol{x} \in \}$. Let $\mathbb{M}^{\mathrm{sym}}$ be the associated state space, which is the subset of the set of real (6×6) symmetric positive-definite matrices satisfying the invariance properties defined by the symmetry group. The information theoretic modeling of elasticity random fields has attracted much attention over the last two decades, starting from the seminal work presented in [40] for purely anisotropic materials (with values in the triclinic symmetry class) to the latest unified results for all symmetry classes presented in [41]; see [42] for a review, as well as [43–47] for other relevant contributions. Other modeling efforts can be found in [48, 49], while more general spectral representations were obtained in the series of papers [50–53] (see [53] for a review). Note that this modeling task is intrinsically different from the construction of methods to properly compute samples of mesoscopic elasticity fields and study convergence towards homogenized properties; readers interested in that topic are referred to [35] for a state-of-the-art introduction.

Regarding the representation of the elasticity tensor, it is convenient to introduce a regularization to ensure a uniform coercivity condition. This can be obtained by letting

$$[\boldsymbol{C}(\boldsymbol{x})] = \frac{1}{1+\varepsilon}[\underline{C}]^{1/2}\{[I_6] + \varepsilon[\boldsymbol{M}(\boldsymbol{x})]\}[\underline{C}]^{1/2}, \quad \boldsymbol{x} \in , \tag{11}$$

for instance, with $[\underline{C}] = \mathbb{E}\{[\boldsymbol{C}(\boldsymbol{x})]\}$, ε a small arbitrary parameter and $\varepsilon > 0$, or by writing

$$[\boldsymbol{C}(\boldsymbol{x})] = [C_0] + (\varepsilon[\underline{C}(\boldsymbol{x})] - [C_0])^{1/2}[\boldsymbol{M}(\boldsymbol{x})] \times (\varepsilon[\underline{C}(\boldsymbol{x})] - [C_0])^{1/2}, \quad \boldsymbol{x} \in , \tag{12}$$

where $[C_0] \in \mathbb{M}^{\mathrm{LB}} \in \mathbb{M}^{\mathrm{sym}}$ is a deterministic lower bound that can be defined through, e.g., multiscale considerations (using energetic bounds). In both cases, $\{[\boldsymbol{M}(\boldsymbol{x})], \boldsymbol{x} \in \}$ is an auxiliary, normalized elasticity field with values in $\mathbb{M}^{\mathrm{sym}}$ such that

$$\mathbb{E}\{[\boldsymbol{M}(\boldsymbol{x})]\} = [I_6] \tag{13}$$

by construction. In addition, it is necessary to introduce a constraint to ensure the well-posedness of the associated stochastic boundary value problem. This can be achieved by imposing

$$\mathbb{E}\{\log(\det([\boldsymbol{M}(\boldsymbol{x})]))\} = \chi, \quad |\chi| < +\infty, \tag{14}$$

where the right-hand side is assumed homogeneous, without loss of generality [40]. The next methodological step then consists in introducing an *ad-hoc* tensor decomposition in $\mathbb{M}^{\mathrm{sym}}$:

$$[\boldsymbol{M}(\boldsymbol{x})] = \sum_{i=1}^{n} M_i(\boldsymbol{x})[E_i], \tag{15}$$

where $\{M_i(\boldsymbol{x}), \boldsymbol{x} \in \}$, $1 \le i \le n$, are scalar-valued ran-dom fields and $\{[E_i(\boldsymbol{x})]\}^n_{i=1}$ constitutes the Walpole basis of $\mathbb{M}^{\mathrm{sym}}$ in Voigt form (note that this basis can be made spatially-varying when the application is such that the crystallographic

orientation defining the symmetry class depends on location) [54]. Let $\{\boldsymbol{M}(\boldsymbol{x}) = (M_1(\boldsymbol{x}), \ldots, M_n(\boldsymbol{x}))^T, \boldsymbol{x} \in \}$ be the vector-valued random field gathering all components in the Walpole expansion (15). The latter defines a symbolic representation that reflects the underlying structure of $\mathsf{M}^{\mathrm{sym}}$ [54] and can be leveraged to derive closed-form results for all symmetry classes. Specific examples relevant to the application under consideration are provided in Sect. 3.2.

Following the previously cited works, we consider classes of translation random fields [55] where the random field $\{\boldsymbol{M}(\boldsymbol{x}), \boldsymbol{x} \in \}$ is sought in the form

$$\boldsymbol{M}(\boldsymbol{x}) = T((\boldsymbol{x})), \quad \forall \boldsymbol{x} \in , \tag{16}$$

where $\{(\boldsymbol{x}), \boldsymbol{x} \in \mathsf{R}^d\}$ is a normalized Gaussian random field with values in R^n and T is a measurable mapping, usually referred to as a transport map in the literature of Bayesian inference, such that

$$\boldsymbol{M}(\boldsymbol{x}) \sim \pi, \tag{17}$$

with π a target probability measure. We assume that π can be represented by a probability density function f with respect to the Lebesgue measure $d\boldsymbol{m} = dm_1 \ldots dm_n$ in R^n, that is, $\pi(d\boldsymbol{m}) = f(\boldsymbol{m})\, d\boldsymbol{m}$.

The stochastic modeling of the random field of material parameters then involves two steps:

1. The first step involves the construction of the latent Gaussian random field $\{(\boldsymbol{x}), \boldsymbol{x} \in \mathsf{R}^d\}$.
2. The second step is focused on the definition of the transport map T.

Important results regarding these two steps are recalled in the next two sections for the sake of self-containedness.

3.1.1 Definition of the latent Gaussian field

In order to perform random sampling on the geometry shown in Fig. 1a, we define the *independent* components of the latent vector-valued Gaussian field $\{(\boldsymbol{x}), \boldsymbol{x} \in \}$ by using the so-called stochastic partial differential equation (SPDE) approach proposed by Lindgren et al.; see [56] for the seminal contribution, as well as [57] for a recent review. The formulation is based on the observation, made by Whittle [58, 59], that a scalar Matérn Gaussian random field (taken here as the jth component of $\{(\boldsymbol{x}), \boldsymbol{x} \in \}$) can be implicitly defined as the solution to a particular SPDE, written in its anisotropic form [60] as

$$\kappa^2 - \nabla \cdot [H^{(j)}(\boldsymbol{x})] \nabla^{\alpha/2} \, {}_j(\boldsymbol{x}) = W(\boldsymbol{x}), \quad \boldsymbol{x} \in \mathsf{R}^d, \tag{18}$$

where κ is a model parameter, $\cdot, \cdot$ is the Euclidean inner product in R^d, ∇ is the nabla (del) operator, $[H]$ is termed the diffusion field, $\alpha = \nu + d/2$ (with ν the smoothness parameter in the associated Matérn covariance function), and $\{\dot{W}(\boldsymbol{x}), \boldsymbol{x} \in \mathsf{R}^d\}$ is the normalized Gaussian white noise. In [56], the authors proposed a Markov approximation that benefits from ease of numerical implementation and was used in many papers (see, e.g., [29, 41, 61–72]), especially within the context of Bayesian inference where the SPDE is used to regularize in the infinite-dimensional setting [57]. Notice that solving Eq. (18) on bounded domains requires the choice of appropriate boundary conditions. Homogeneous Neumann boundary conditions were used in [56], while the use of other boundary conditions was investigated in [61, 73, 74] to circumvent folding boundary effects.

Of particular interest in the present work is the capability of the formulation to account for geometrical complexity through the definition of the diffusion field [29, 41, 68–70]. In practice, the diffusion coefficient can be defined as

$$[H^{(j)}(\boldsymbol{x})] = \sum_{i=1}^{d} \lambda_i^{(j)} \boldsymbol{e}_i^{(i)}(\boldsymbol{x}) \otimes \boldsymbol{e}_i^{(i)}(\boldsymbol{x}), \quad \forall \boldsymbol{x} \in , \tag{19}$$

where $\{\lambda_i^{(j)} > 0\}_{i=1}^d$ are parameters that control the anisotropy and correlation lengths in the covariance function of the latent Gaussian field $\{ {}_j(\boldsymbol{x}), \boldsymbol{x} \in \}$, $1 \le j \le n$, and $\{\boldsymbol{x} \to \boldsymbol{e}_i^{(i)}(\boldsymbol{x})\}_{i=1}^d$ are called orientation, or directional, fields. These fields define the directions of local filtering for the Gaussian white noise, and can be either inferred from processing conditions, when laser deposition paths can be tracked, or by using application-dependent fictitious flow problems [69]. In the latter case, each field can be defined as

$$\boldsymbol{e}_i^{(i)}(\boldsymbol{x}) = \frac{1}{\nabla_i(\boldsymbol{x})} \nabla_T(\boldsymbol{x}), \quad \forall \boldsymbol{x} \in , \quad 1 \le i \le d, \tag{20}$$

where ${}_i$ is the solution to the Laplace equation

$$(\boldsymbol{x}) = 0, \quad \forall \boldsymbol{x} \in , \tag{21}$$

which is supplemented with problem- and component-specific Dirichlet boundary conditions, defined to drive the flow along desired paths, and Neumann boundary conditions that enforce the normal component of the flow velocity to vanish at interfaces with geometrical features. This approach will be exemplified in Sect. 5.

3.2 Transport maps for isotropic and orthotropic elasticity tensors

3.2.1 Isotropic model

Following [54], the normalized elasticity tensor $[\boldsymbol{M}(\boldsymbol{x})]$ with values in the set $\mathbb{M}^{\mathrm{iso}}$ of isotropic tensors admits the representation

$$[\boldsymbol{M}(\boldsymbol{x})] = \{M_1(\boldsymbol{x}), M_2(\boldsymbol{x})\}, \tag{22}$$

where $M_1 = 3k$ and $M_2 = 2\mu$, with k and μ the bulk and shear moduli. As previously indicated, the above representation is introduced in order to perform algebraic calculations in a particularly simple way. For instance, the symbolic representation for the inverse reads as

$$[\boldsymbol{M}(\boldsymbol{x})]^{-1} = \{M_1(\boldsymbol{x})^{-1}, M_2(\boldsymbol{x})^{-1}\}, \tag{23}$$

while the action of any polynomial transformation $\mathbb{P}$ can be decomposed as

$$\mathbb{P}([\boldsymbol{M}(\boldsymbol{x})]) = \{\mathbb{P}(M_1(\boldsymbol{x})), \mathbb{P}(M_2(\boldsymbol{x}))\}. \tag{24}$$

Notice that similar properties hold for all symmetry class [54]. Considering the constraints given by Eqs. (13–14) in a maximum entropy principle formulation [75, 76], it can be deduced that

$$\pi = \pi_{M_1} \otimes \pi_{M_2} \tag{25}$$

where π_{M_1} and π_{M_2} are Gamma probability distributions [44]. It follows that

$$k(\boldsymbol{x}) = T_1\{\ _1(\boldsymbol{x})\}, \quad \mu(\boldsymbol{x}) = T_2\{\ _2(\boldsymbol{x})\}, \quad \forall \boldsymbol{x} \in \Omega, \tag{26}$$

where the transport maps are defined by

$$T_1 = F^{-1}_{G(a_1,\ b_1)} \circ F_{N(0,1)} \tag{27}$$

and

$$T_2 = F^{-1}_{G(a_2,\ b_2)} \circ F_{N(0,1)}. \tag{28}$$

In the above equations:

- $F_{G(a,b)}$ is the cumulative distribution function of the Gamma law with with a and b as scale and shape parameters, respectively;
- $F_{N(0,1)}$ is the cumulative distribution function of the standard Gaussian law; and
- $\{\ _1(\boldsymbol{x}), \boldsymbol{x} \in \Omega\}$ and $\{\ _2(\boldsymbol{x}), \boldsymbol{x} \in \Omega\}$ are the two mutu-ally independent components of the latent Gaussian field $\{(\boldsymbol{x}), \boldsymbol{x} \in \Omega\}$, defined as solutions to the SPDE pre-sented in Sect. 3.1.1.

Notice that marginal inter-correlation between the moduli can be introduced [77].

3.2.2 Orthotropic model

Assume now that the normalized elasticity field takes values in the set $\mathbb{M}^{\mathrm{ort}}$ of orthotropic tensors defined by the given mutually orthogonal unit vectors $\boldsymbol{a}$, $\boldsymbol{b}$, and $\boldsymbol{c}$. The random field $\{[\boldsymbol{M}(\boldsymbol{x})], \boldsymbol{x} \in \Omega\}$ can similarly be expanded as

$$[\boldsymbol{M}(\boldsymbol{x})] = \sum_{i=1}^{9} M_i(\boldsymbol{x})\,[E_i], \tag{29}$$

where the Walpole basis corresponds to the Voigt representation of the following fourth-order tensors

$$E_1 = \boldsymbol{a} \otimes \boldsymbol{a} \otimes \boldsymbol{a} \otimes \boldsymbol{a},\ E_2 = \boldsymbol{b} \otimes \boldsymbol{b} \otimes \boldsymbol{b} \otimes \boldsymbol{b},\ E_3 = \boldsymbol{c} \otimes \boldsymbol{c} \otimes \boldsymbol{c} \otimes \boldsymbol{c}, \tag{30}$$

$$\begin{aligned} E_4 &= \boldsymbol{a} \otimes \boldsymbol{a} \otimes \boldsymbol{b} \otimes \boldsymbol{b} + \boldsymbol{b} \otimes \boldsymbol{b} \otimes \boldsymbol{a} \otimes \boldsymbol{a}, \\ E_5 &= \boldsymbol{b} \otimes \boldsymbol{b} \otimes \boldsymbol{c} \otimes \boldsymbol{c} + \boldsymbol{c} \otimes \boldsymbol{c} \otimes \boldsymbol{b} \otimes \boldsymbol{b}, \\ E_6 &= \boldsymbol{a} \otimes \boldsymbol{a} \otimes \boldsymbol{c} \otimes \boldsymbol{c} + \boldsymbol{c} \otimes \boldsymbol{c} \otimes \boldsymbol{a} \otimes \boldsymbol{a}, \end{aligned} \tag{31}$$

and

$$\begin{aligned} E_7 &= (\boldsymbol{a} \otimes \boldsymbol{b} + \boldsymbol{b} \otimes \boldsymbol{a}) \otimes (\boldsymbol{a} \otimes \boldsymbol{b} + \boldsymbol{b} \otimes \boldsymbol{a})/2\ , \\ E_8 &= (\boldsymbol{b} \otimes \boldsymbol{c} + \boldsymbol{c} \otimes \boldsymbol{b}) \otimes (\boldsymbol{b} \otimes \boldsymbol{c} + \boldsymbol{c} \otimes \boldsymbol{b})/2, \\ E_9 &= (\boldsymbol{c} \otimes \boldsymbol{a} + \boldsymbol{a} \otimes \boldsymbol{c}) \otimes (\boldsymbol{c} \otimes \boldsymbol{a} + \boldsymbol{a} \otimes \boldsymbol{c})/2. \end{aligned} \tag{32}$$

The random field of elasticity tensor is then written in terms of the symbolic form as

$$[\boldsymbol{M}(\boldsymbol{x})] = \{[\boldsymbol{N}(\boldsymbol{x})], M_7(\boldsymbol{x}), M_8(\boldsymbol{x}), M_9(\boldsymbol{x})\}. \tag{33}$$

where $[\boldsymbol{N}(\boldsymbol{x})]$ is the random matrix defined as

$$[\boldsymbol{N}(\boldsymbol{x})] = \begin{bmatrix} M_1(\boldsymbol{x}) & M_4(\boldsymbol{x}) & M_6(\boldsymbol{x}) \\ M_4(\boldsymbol{x}) & M_2(\boldsymbol{x}) & M_5(\boldsymbol{x}) \\ M_6(\boldsymbol{x}) & M_5(\boldsymbol{x}) & M_3(\boldsymbol{x}) \end{bmatrix}. \tag{34}$$

Using the rules of algebraic operations in $\mathbb{M}^{\mathrm{ort}}$ [54], it can be shown that the constraints defined by Eqs. (13–14) are equivalent to [41]

$$\mathbb{E}\{[\boldsymbol{N}(\boldsymbol{x})]\} = [I_3], \quad \mathbb{E}\{M_i(\boldsymbol{x})\} = 1, \quad i = 7, 8, 9, \quad \forall \boldsymbol{x} \in \Omega, \tag{35}$$

together with

$$\mathbb{E}\{\log(\det([\boldsymbol{N}(\boldsymbol{x})]))\} = \chi, \quad |\chi| < +\infty, \quad \forall \boldsymbol{x} \in \Omega. \tag{36}$$

and

$$\mathbb{E}\{\log(M_i(\boldsymbol{x}))\} = \chi_i, \quad |\chi_i| < +\infty, \; i = 7,8,9, \quad \forall \boldsymbol{x} \in D. \tag{37}$$

Under the above constraints, it can be deduced that

$$\pi = \pi_{[N]} \otimes \pi_{M_7} \otimes \pi_{M_8} \otimes \pi_{M_9} \tag{38}$$

where

- $\pi_{[N]}$ is defined by the probability density function [78]

$$p_{[N]}([n]) = \mathbb{1}_{\mathbb{R}_0^{3\times 3}}([n])\, c\, (\det([n]))^{2(1-\delta_{[N]}^2)/\delta_{[N]}^2} \times \exp\left(-\frac{2}{\delta_{[N]}^2}\mathrm{tr}([n])\right), \tag{39}$$

  where $\mathbb{1}_{\mathbb{R}_0^{3\times 3}}$ is the indicator function of the set of 3×3 real positive-definite symmetric matrices, c is the normalization constant and $\delta_{[N]}$ is the coefficient of variation of $[\boldsymbol{N}(\boldsymbol{x})]$ defined as

$$\delta_{[N]} = \frac{1}{3}\mathbb{E}\{\|[\boldsymbol{N}(\boldsymbol{x})] - [I_3]\|_F^2\}^{1/2}; \tag{40}$$

- π_{M_i}, $i = 7,8,9$, is a Gamma probability distribution, with shape and scale parameters denoted by a_i and b_i, respectively.

Notice that the above probability measures correspond to the first-order marginal distributions for the random fields (and hence define the transport map T), and that the coefficients of variation of the components in the symbolic form are related to the coefficient of variation of $[\boldsymbol{M}]$ through [41]

$$\delta_{[M]} = \frac{1}{6}\left(3\delta_{[N]}^2 + \delta_{M_7}^2 + \delta_{M_8}^2 + \delta_{M_9}^2\right)^{1/2}. \tag{41}$$

Using the results derived in [78], it can further can be shown that $[\boldsymbol{N}(\boldsymbol{x})]$ admits the factorization

$$[\boldsymbol{N}(\boldsymbol{x})] = [\boldsymbol{L}(\boldsymbol{x})]^T[\boldsymbol{L}(\boldsymbol{x})], \tag{42}$$

where for $\boldsymbol{x}$ fixed in D, $[\boldsymbol{L}(\boldsymbol{x})]$ is an upper-triangular random matrix, the components of which are defined as

$$L_{11}(\boldsymbol{x}) = \frac{\delta_{[N]}}{2}\sqrt{2}F^{-1}_{G\left(\frac{1}{\delta_{[N]}^2}, 1\right)}(F_{N(0,1)}(\xi_1(\boldsymbol{x}))), \tag{43}$$

$$L_{22}(\boldsymbol{x}) = \frac{\delta_{[N]}}{2}\sqrt{2F^{-1}_{G\left(\frac{1}{\delta_{[N]}^2}+\frac{1}{2}, 1\right)}(F_{N(0,1)}(\xi_2(\boldsymbol{x})))}, \tag{44}$$

$$L_{33}(\boldsymbol{x}) = \frac{\delta_{[N]}}{2}\sqrt{2F^{-1}_{G\left(\frac{1}{\delta_{[N]}^2}+\frac{3}{2}, 1\right)}(F_{N(0,1)}(\xi_3(\boldsymbol{x})))}, \tag{45}$$

$$L_{12}(\boldsymbol{x}) = \frac{\delta_{[N]}}{2}\xi_4(\boldsymbol{x}), \tag{46}$$

$$L_{13}(\boldsymbol{x}) = \frac{\delta_{[N]}}{2}\xi_6(\boldsymbol{x}), \tag{47}$$

and

$$L_{23}(\boldsymbol{x}) = \frac{\delta_{[N]}}{2}\xi_5(\boldsymbol{x}). \tag{48}$$

In addition, we have that

$$M_7(\boldsymbol{x}) = F^{-1}_{G(a_7,b_7)}(F_{N(0,1)}(\xi_7(\boldsymbol{x}))), \tag{49}$$

$$M_8(\boldsymbol{x}) = F^{-1}_{G(a_8,b_8)}(F_{N(0,1)}(\xi_8(\boldsymbol{x}))), \tag{50}$$

and

$$M_9(\boldsymbol{x}) = F^{-1}_{G(a_9,b_9)}(F_{N(0,1)}(\xi_9(\boldsymbol{x}))). \tag{51}$$

In the above equations, $\{\{\xi_j(\boldsymbol{x}), \boldsymbol{x} \in D\}\}_{j=1}^9$ are statistically independent standard Gaussian random fields, taking values in $\mathbb{R}$ and indexed by D, defined as the solution to the SPDE presented in Sect. 3.1.1. The combination of Eqs. (42–51) explicitly defines the transport map T pushing forward the tensorization of the normalized Gaussian probability measures, for $\boldsymbol{x}$ fixed in D, to the information-theoretic non-Gaussian measure π.

4 Model calibration

4.1 Calibration of the first-order marginal distribution

The goal of this section is to identify the hyperparameters defining the measures π_{M_1} and π_{M_2} for the isotropic model presented in Sect. 3.2.1, and the measures $\pi_{[N]}$, π_{M_7}, π_{M_8}, and π_{M_9} for the orthotropic model introduced in Sect. 3.2.2.

4.1.1 Results for the isotropic model

Since the bulk and shear moduli are marginally Gamma distributed, hyperparameters in π_{M_1} and π_{M_2} can be obtained as

$$a_{M_1} = a_k, \quad b_{M_1} = 3b_k, \tag{52}$$

and

$$a_{M_2} = a_\mu, \quad b_{M_2} = 2b_\mu, \tag{53}$$

respectively, where a_k, b_k, a_μ, and b_μ can be estimated either through spatial averaging (ergodic estimator) or by the maximum likelihood method. These values, computed through averaging, are reported in Table 1 for all three metrics.

Small fluctuations (less than 1%) are typically observed for both moduli, with the stochastic shear modulus exhibiting more fluctuations than the bulk modulus. Kernel density estimations for the first-order marginal distributions (based on 2,000 independent samples) of elasticity tensor components are shown in Fig. 7.

4.1.2 Results for the orthotropic model

Using the experimental database described in Sect. 2.2, it is found that the mean tensor for the elasticity field is

$$[\underline{C}] = \begin{matrix} 282.5600 & 106.3067 & 115.2733 \\ 106.3067 & 283.9333 & 113.8867 \\ 115.2733 & 113.8867 & 274.9667 \end{matrix}, \begin{matrix} 74.8733, & 81.4667, & 83 \end{matrix} \quad (54)$$

in [GPa]. In addition, dispersion parameters are obtained as follows: $\delta_{[\boldsymbol{N}]} = 3.18\%$, $\delta_{M_7} = 5.16\%$, $\delta_{M_8} = 2.88\%$, and $\delta_{M_9} = 2.86\%$. Using Eq. (41), we deduce that $\delta_{[\boldsymbol{M}(s)]} = 3.5\%$. These results have to be compared with the ones provided in Sect. 4.1.1, and it is seen that the orthotropic model exhibit much larger fluctuations than the isotropic approximation. This indicates that preserving the material symmetry is key to properly capturing the statistical fluctuations. It should also be kept in mind that the level of fluctuations strongly depends on the size of the domain where EBSD measurements take place (and where homogenization is performed): the larger the domain size, the smaller the fluctuations—owing to the separation of scales.

In addition, kernel density estimations for the first-order marginal probability density functions are provided in Fig. 8. In this figure, the red markers represent the experimental samples obtained by combining EBSD data with the homogenization procedure.

It is seen, in particular, that non-vanishing probability levels are obtained for all samples, and that the spread of the data is well captured.

4.2 Calibration of the spatial correlation length

In this section, we address the partial calibration of the covariance structure based on the spatial sampling described in Sect. 2. Since only one realization of the field is available, an ad-hoc identification strategy is first proposed in Sect. 4.2.1. Results for the isotropic and orthotropic models are subsequently presented in Sects. 4.2.2 and 4.2.3, respectively.

4.2.1 Strategy

To facilitate the description of the correlation structure in accordance with both the geometry and processing conditions, we introduce a curvilinear coordinate system $\boldsymbol{s} = (s_1, s_2, s_3)^T$, associated with the shell domain where characterization occurs. Specifically, s_3 denotes the curvilinear coordinate along the path $_{s_3}$ highlighted with a red solid line in the right panel in Fig. 1a, and (s_1, s_2) are the in-plane curvilinear coordinates in the $x - y$ Cartesian plane. In order to perform the calibration of the correlation length along $_{s_3}$, the translation model is written in terms of the curvilinear system

$$\boldsymbol{M}(\boldsymbol{s}) = T((\boldsymbol{s})), \quad \forall \boldsymbol{x} \in \boldsymbol{s}, \quad (55)$$

where $\boldsymbol{s} = (0, 0, s_3)^T$. Note that the change in the index set (from to $_{\boldsymbol{s}}$) does not imply a change of coordinate system for the elasticity tensor itself. We then consider the random field $\{\boldsymbol{M}(s_3), s_3 \in {}_s{}_3\}$, with a slight abuse of notation, and denote by $s_3 \to \boldsymbol{m}^{\exp}(s_3)$ the experimental sample obtained by combining the EBSD measurements with the homogenization approach (components of this sample can be seen in Fig. 6 for the isotropic approximation, for instance). For a given transport map T (or equivalently, for a given symmetry class), the associated realization $s_3 \to \xi^{\exp}(s_3)$ of the (restriction of the) latent Gaussian field can be computed as

$$\xi^{\exp}(s_3) = T^{-1}(\boldsymbol{m}^{\exp}(s_3)), \quad \forall s_3 \in {}_{s_3}. \quad (56)$$

Upper bounds for the correlation lengths $\{L_3^{(j)} > 0\}_{j=1}^n$ (with $n = 2$ and $n = 9$ for the isotropic and orthotropic cases, respectively) can then be identified as follows.

Consider the identification of an upper bound $\overline{L}_3^{(k)}$, $1 \le k \le n$, associated with the kth component $\{ {}_k(s_3), s_3 \in {}_{s_3}\}$ of $\{(s_3), s_3 \in {}_{s_3}\}$. Let $\xi^{\exp,k}$ be the (deterministic) vector gathering the realization of $\{ {}_k(s_3), s_3 \in {}_{s_3}\}$ at the N_p sampled points. Let $\{ {}^{\mathrm{mod}}(s_3), s_3 \in {}_{s_3}\}$ be a scalar-valued, centered Matérn Gaussian random field indexed by the same one-dimensional domain $_{s_3}$, with $\alpha = 1/2$ and correlation length L. Notice that a Matérn covariance function is chosen here—without loss of generality—since the latent Gaussian fields will ultimately be simulated with the SPDE approach recalled in Sect. 3.1.1. Similarly, let ${}^{\mathrm{mod}}(L)$ be the Gaussian random vector gathering the values of $\{ {}^{\mathrm{mod}}(s_3), s_3 \in {}_{s_3}\}$ at the N_p sampled points, where the dependence on L is made explicit in order to derive the calibration optimization problem. Introduce now a partition

$${}^{\mathrm{mod}}(L) = \begin{matrix} {}_1^{\mathrm{mod}}(L) \\ {}_2^{\mathrm{mod}}(L) \end{matrix}, \quad (57)$$

Table 1 Estimated mean values and coefficients of variation of the elastic moduli corresponding to the isotropic approximation computed with the Euclidean (E), Log-Euclidean (L-E), and Riemannian (R) metrics

Parameter	Mean (GPa)	CV (%)	Scale parameter a	Shape parameter
k (E)	168.0439	0.1044	917131.7922	0.000183228
μ (E)	81.6010	0.4637	46515.1194	0.00175429
k (L-E)	168.0438	0.1044	916760.2112	0.000183302
μ (L-E)	81.4251	0.4491	49586.0267	0.00164210
k (R)	168.0438	0.1044	916760.2112	0.000183302
μ (R)	81.4251	0.4491	49586.0267	0.00164210

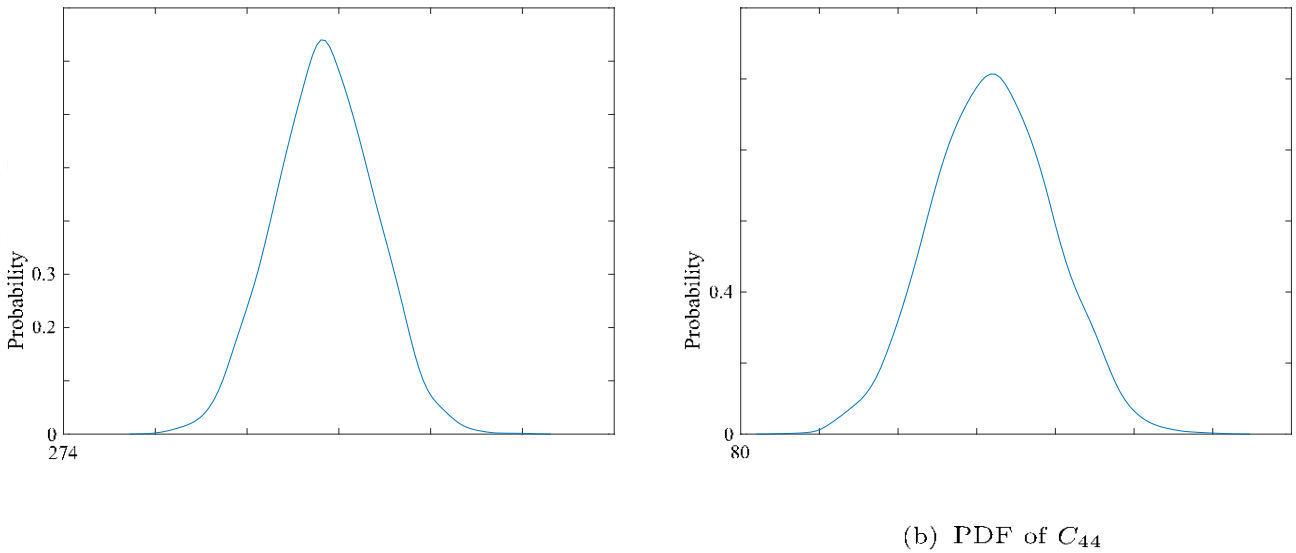

(b) PDF of C_{44}

Fig. 7 (First-order marginal) Probability density functions of C_{11} and C_{44} (in [GPa]) for the isotropic case, estimated with 2,000 samples. Experimental mean values for these components (after projections onto the set of isotropic tensors) are 276.8451 [GPa] and 81.6010 [GPa], respectively (see Table 1)

where $^{\mathrm{mod}}_{1}(L)$ and $^{\mathrm{mod}}_{2}(L)$ are random vectors of lengths $(N_p - N_f)$ and N_f, respectively. This partition is constructed by selecting a set of N_f points amongst the N_p points where samples were collected. Let

$$\xi^{\mathrm{exp},k} = \begin{matrix} \xi^{\mathrm{exp},k}_{1} \\ \xi^{\mathrm{exp},k}_{2} \end{matrix} \tag{58}$$

be the associated partition for the experimental data. Owing to the Gaussianity of $^{\mathrm{mod}}(L)$, it follows that the distribution of $^{\mathrm{mod}}_{1}(L) \,|\, ^{\mathrm{mod}}_{2}(L) = \xi_e^{\mathrm{xp},k}$ is

$$\mathcal{N}\left([^{\mathrm{mod}}_{12}(L)][^{\mathrm{mod}}_{22}(L)]^{-1}\xi_e^{\mathrm{xp},k}{}_2,\ [^{\mathrm{mod}}_{11}(L)] - [^{\mathrm{mod}}_{12}(L)][^{\mathrm{mod}}_{22}(L)]^{-1}[^{\mathrm{mod}}_{21}(L)]\right), \tag{59}$$

where $\mathcal{N}$ denotes the Gaussian distribution and

$$[^{\mathrm{mod}}(L)] = \begin{matrix} [^{\mathrm{mod}}_{11}(L)] & [^{\mathrm{mod}}_{12}(L)] \\ [^{\mathrm{mod}}_{21}(L)] & [^{\mathrm{mod}}_{22}(L)] \end{matrix} \tag{60}$$

is the covariance matrix of $^{\mathrm{mod}}(L)$, the block structure of which is induced by the partition in Eq. (57). An upper bound for the correlation length $L_3^{(k)}$ can then be identified by the maximum likelihood method, that is,

$$\overline{L}_3^{(k)} = \mathrm{argmax}_{L>0} \prod_{j=1}^{N_p - N_f} f_{^{\mathrm{mod}}_{1,j}(L)}(\xi_{1,j}^{\mathrm{xp},k}), \tag{61}$$

where $\xi_{1,j}^{\mathrm{exp},k}$ is the jth component of $\xi_e^{\mathrm{xp},k}$ and the probability density function $f_{^{\mathrm{mod}}_{1,j}(L)}$ defining the jth component of $^{\mathrm{mod}}_{1}(L)$ is computed by a kernel density estimation (for a given L).

Intuitively, values of L that are larger than the sought-after correlation length yield low likelihood values (with a monotonic decrease trend), since spatial variations cannot be captured accurately, while minor fluctuations and/or a plateau can be expected for values that are smaller than the most plausible value of the correlation length—hence the consideration of upper bounds, rather than point estimates. The choice of the N_f points upon which conditioning is performed is therefore of paramount importance. In practice, this choice is guided by the local monotonicity of the experi-

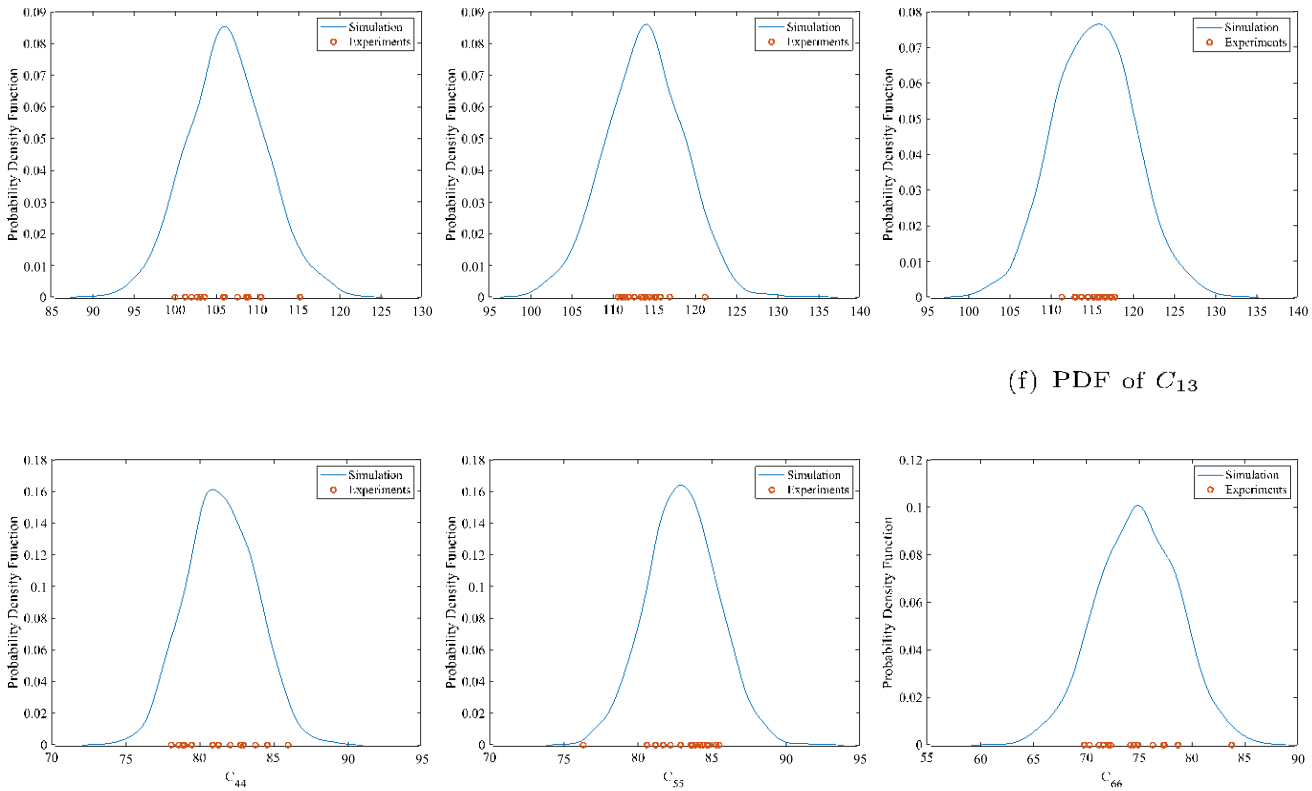

(f) PDF of C_{13}

(g) PDF of C_{44} (h) PDF of C_{55} (i) PDF of C_{66}

Fig. 8 (First-order marginal) Probability density functions of the elasticity matrix components (in [GPa]) for the orthotropic case, estimated with 2,000 samples. Realizations obtained by combining the experiments (EBSD) and the multiscale approach are shown using red circular markers

mental sample, so that non-negligible variations are observed around the N_f selected points, as well as by the sensitivity of the maximum likelihood estimator.

4.2.2 Results for the isotropic model

We now deploy the method presented in Sect. 4.2.1 to identify plausible correlation ranges for the isotropic model. The experimental samples of the bulk and shear moduli, denoted by $s_3 \to k^{\exp}(s_3)$ and $s_3 \to \mu^{\exp}(s_3)$ respectively, are first pulled back according to

$$\xi_1^{\exp}(s_3) = T_1^{-1}\{k^{\exp}(s_3)\},$$
$$\xi_2^{\exp}(s_3) = T_2^{-1}\{\mu^{\exp}(s_3)\}, \quad \forall s_3 \in s_3, \tag{62}$$

where T_1 and T_2 are defined in Eqs. (27–28), with the parameters identified in Sect. 4.1.1. The experimental samples thus obtained are shown in Fig. 9, for the case of an isotropic approximation defined by the Euclidean metric. Notice that the choice of the latter metric is not expected to impact

the prediction in terms of correlation lengths, given that the wavelengths of the spatial fluctuations were found to be insensitive to the projection metric (see Fig. 6a, b).

Figure 10a and b show the points that were chosen for conditioning (red circles), as well as the points where the likelihood function was evaluated.

The graphs of the log-likelihood functions associated with the computation of $L_3^{(1)}$ and $L_3^{(2)}$ are shown in Fig. 11a and b, respectively.

The likelihood function behaves as expected in both cases, exhibiting a plateau for small correlation lengths and a sharp decrease as the correlation length increases. It is found that $\overline{L}_3^{(1)} = 24$ and $\overline{L}_3^{(2)} = 26$ [mm], suggesting similar correlation ranges for the two elastic moduli along the curvilinear path.

4.2.3 Results for the orthotropic model

A similar approach can be followed to identify upper bounds for the correlation lengths along s_3 in the orthotropic case. Specifically:

1. The realization $s_3 \to [C^{\exp}(s_3)]$ of the elasticity field is first normalized in mean to estimate the sample of $s_3 \to [M^{\exp}(s_3)]$, using spatial averaging for the components in Walpole's symbolic form.
2. The realizations of the latent Gaussian fields are next computed by pulling back the samples of the components, namely $s_3 \to [N^{\exp}(s_3)]$ and $s_3 \to m_i^{\exp}(s_3)$ for $7 \le i \le 9$, using Eqs. (43–51). For instance, one has

$$\xi_1^{\exp}(s_3) = F^{-1}_{N(0,1)}\left(F_{G\left(\frac{2}{\delta_{[N]}^2},1\right)}\left(\frac{1}{2}\,\frac{2}{\delta_{[N]}}\, l_{\mathrm{bl}}^{\exp}(s_3)\right)^2\right) \tag{63}$$

and

$$\xi_7^{\exp}(s_3) = F^{-1}_{N(0,1)}\left(F_{G(a_7,b_7)}(m_7^{\exp}(s_3))\right), \quad \forall s_3 \in \Omega_{s_3}, \tag{64}$$

where $s_3 \to l_{\mathrm{bl}}^{\exp}(s_3)$ is the realization of $\{L_{11}(s_3), s_3 \in \Omega_{s_3}\}$ computed from the realization $s_3 \to [N^{\exp}(s_3)]$ of $\{[\boldsymbol{N}(s_3)], s_3 \in \Omega_{s_3}\}$ using a Cholesky factorization.
3. Conditional sampling is applied and the maximum likelihood function is used to identify upper bounds for the correlation lengths along the curvilinear coordinate s_3.

The samples of the latent Gaussian fields computed by pulling back the experimental realizations are shown in Fig. 12a (for the components associated with the matrix-valued coefficient $[\boldsymbol{N}(s)]$) and Fig. 12b (for the components associated with the remaining coefficients M_7, M_8, and M_9).

The evolution of the log-likelihood functions are shown for all latent Gaussian random fields in Fig. 13a and b, and upper bounds are provided in Table 2.

It is seen that upper bounds vary greatly between components. It should be kept in mind, however, that the contributions of fields $\{\ _i(s_3), s_3 \in \Omega_{s_3}\}_{i=1}^{6}$ are mixed through the Cholesky factorization (see Eq. (42)), hence making results for these components less interpretable.

5 Material uncertainty propagation

In this section, we exemplify the framework using the calibrated results for the two symmetry classes. The construction of appropriate directional fields is first addressed in Sect. 5.1. Samples of the latent Gaussian and non-Gaussian fields corresponding to calibrated values are shown in Sect. 5.2. Uncertainty propagation is finally performed in Sect. 5.3.

5.1 Problem definition and construction of the directional fields

For illustration purposes, we restrict the analysis to the apex of the tank shown in Fig. 1; see Fig. 14a. An a posteri-ori evaluation of the reduction that can be achieved with a Karhunen-Loève expansion indicates that the stochas-tic reduced dimension remains very high (typically greater than a few hundreds, depending on the energy threshold), especially for the orthotropic case. In this case, stochastic collocation methods can require as many samples as the Monte Carlo method, which is preferred here for its simplicity. To reduce the computational cost associated with the Monte Carlo solver, only a quarter of the apex is modeled due to the symmetry of both the geometry and loading conditions detailed in Sect. 5.3; see Fig. 14b. It is assumed that a properly symmetrized version of the random field is considered over the entire apex, so that symmetry can be invoked.

Following the approach developed in Sect. 3.1.1, the directional field enabling filtering along the curvilinear coordinate s_3 is constructed by solving the Laplace problem with the boundary conditions shown in Fig. 14b. The solution to this problem is obtained by the finite element method, using a mesh comprised of 41,232 P_1 elements and 9,890 nodes, and the associated (normalized) gradient are shown in Fig. 15a and b, respectively.

Note that the directional field is plot at the center point of each element, and that only a few randomly-selected vectors are shown for the sake of illustration. Finally, the other directional fields are taken as

$$\boldsymbol{e}^{(1)}(\boldsymbol{x}) = (1, 0, 0)^T, \quad \boldsymbol{e}^{(2)}(\boldsymbol{x}) = (0, 1, 0)^T, \tag{65}$$

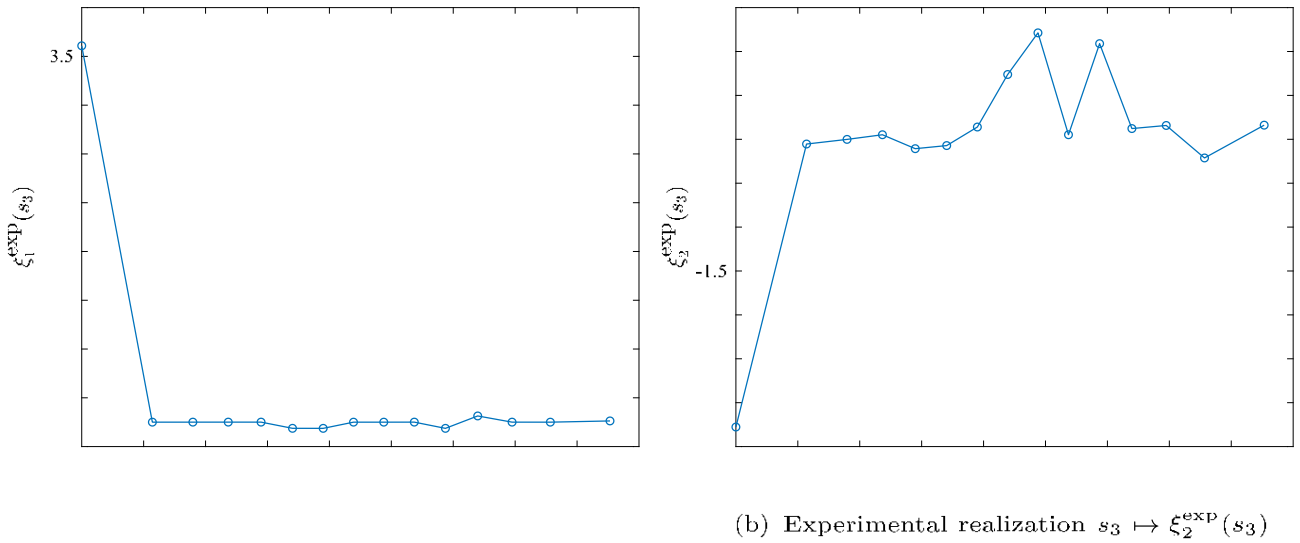

Fig. 9 Experimental realization $s_3 \to \xi_1^{\exp}(s_3)$ and $s_3 \to \xi_2^{\exp}(s_3)$ obtained by pulling back the experimental sample of the bulk modulus random field (Euclidean metric)

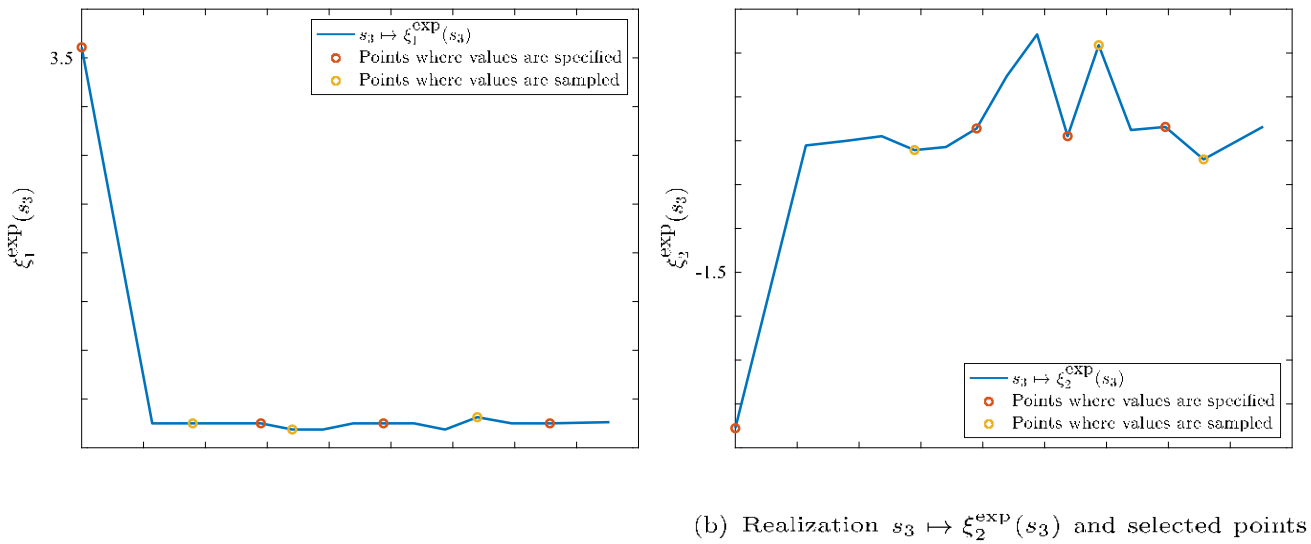

Fig. 10 Realizations $s_3 \to \xi_1^{\exp}(s_3)$ and $s_3 \to \xi_2^{\exp}(s_3)$, points where conditioning is performed (red circles, with $N_f = 4$), and points used in the evaluation of the log-likelihood function (orange circles)

to introduce in-plane filtering, in accordance with processing conditions. The directional fields thus defined are used in the next section to conduct sampling for the elasticity field, using the calibration results obtained in the previous sections.

dummy

5.2 Sampling results

In this section, we invoke the identification results presented in Sects. 4.2.2 and 4.2.3 to perform random sampling on the apex.

5.2.1 Isotropic case

For the isotropic case, two latent Gaussian fields are used to generate samples of the random fields $\{k(\boldsymbol{x}),\ \boldsymbol{x} \in \}$ and $\{\mu(\boldsymbol{x}),\ \boldsymbol{x} \in \}$. The upper bound identified from experiments corresponds to the directional field $\boldsymbol{e}^{(3)}$, and assumptions must be made regarding the other two directions. To qualitatively illustrate the influence of correlation parameters, we assume that $\boldsymbol{L}^{(1)} = \boldsymbol{L}^{(2)}$ (that is, that the two latent Gaussian fields exhibit similar correlation ranges; see [79] therein, in particular Fig. 9, for a multiscale-informed construction) and denote by $\boldsymbol{L} = (L_1, L_2, L_3)^T$ the vector gathering the correlation lengths along the three orientation fields. We fur-

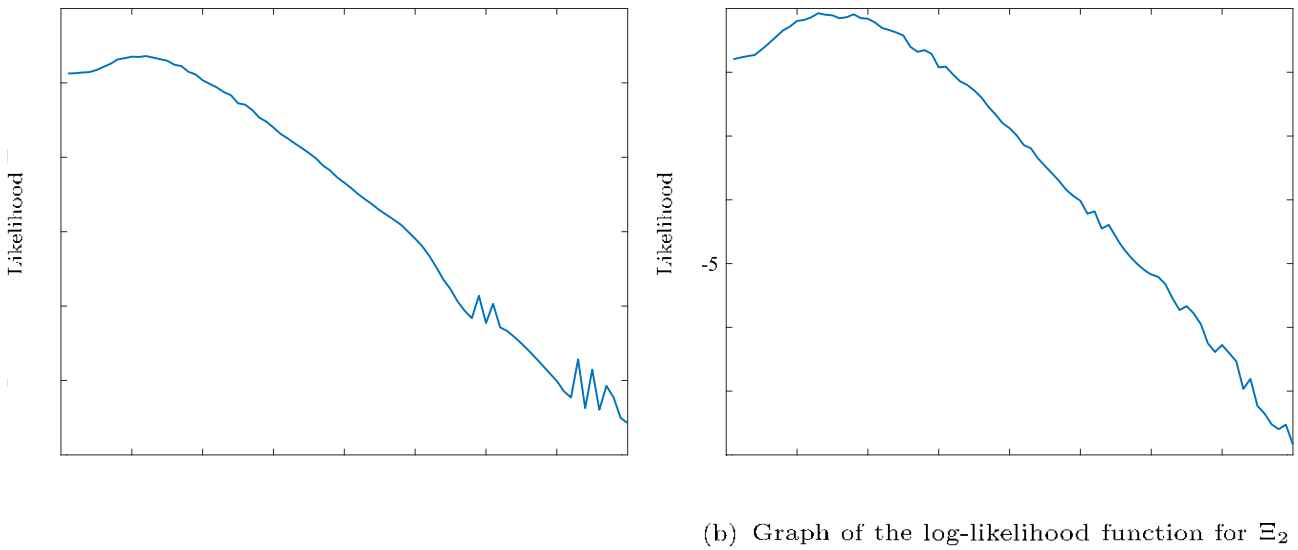

(b) Graph of the log-likelihood function for Ξ_2

Fig. 11 Graphs of the log-likelihood functions for the two components of the latent Gaussian random field

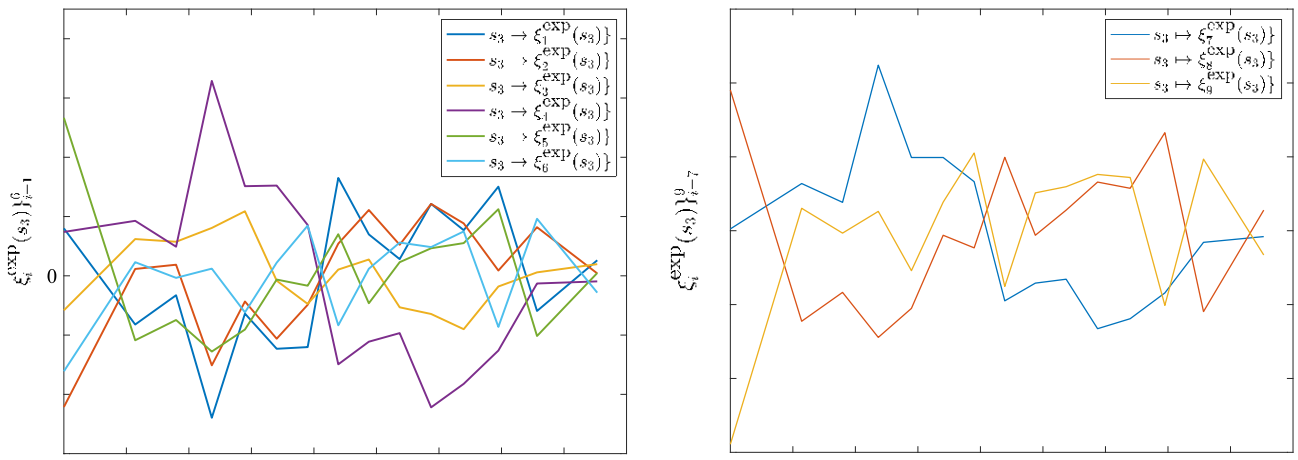

(b) Experimental samples $\{s_3 \mapsto \xi_i^{\exp}(s_3)\}_{i=7}^{9}$

Fig. 12 Experimental samples $\{s_3 \to \xi_i^{\exp}(s_3)\}_{i=1}^{6}$, computed by using Eqs. (42–51)

ther assume that the in-plane correlation lengths are equal, and consider two scenarios. In the first case, the in-place correlation lengths are assumed to be much shorter than the out-of-place correlation lengths: $L_1 = L_2 \ll L_3$, where we take $L_3 = 30$ [mm] following the results presented in Sect. 4.2. In the second scenario, all correlation lengths are set equal [29]. Parameters in the diffusion matrix (see Eq. (19)) are then taken as $\lambda_i = \kappa L_i^2$, where $\kappa = 1$. Associated realizations of the latent Gaussian field $_1$ and bulk shear modulus are shown in Figs. 16 and 17, respectively. A sample of the shear modulus random field can be seen in Fig. 18.

In the first configuration, the anisotropic structure leads to pronounced spatial variations, while the isotropic parameterization in the second scenario yields smoother variations with narrower ranges of fluctuations. Finally, samples of the $C_{11}(\boldsymbol{x}) = k(\boldsymbol{x}) + \frac{4\mu(\boldsymbol{x})}{3}$ can be seen in Fig. 19.

5.2.2 Orthotropic case

In the case of the orthotropic description, nine latent Gaussian random fields $\{\{ _i(\boldsymbol{x}), \boldsymbol{x} \in \Omega \}\}_{i=1}^{9}$ are required to generate the elasticity matrix random field. For a given Gaussian field $\{ _k(\boldsymbol{x}), \boldsymbol{x} \in \Omega \}$, $1 \le k \le 9$, we similarly consider two scenarios where the diffusion kernel is parameterized using

$$\lambda_i = \kappa L_i^{(k)2}, \quad 1 \le i \le 3,$$

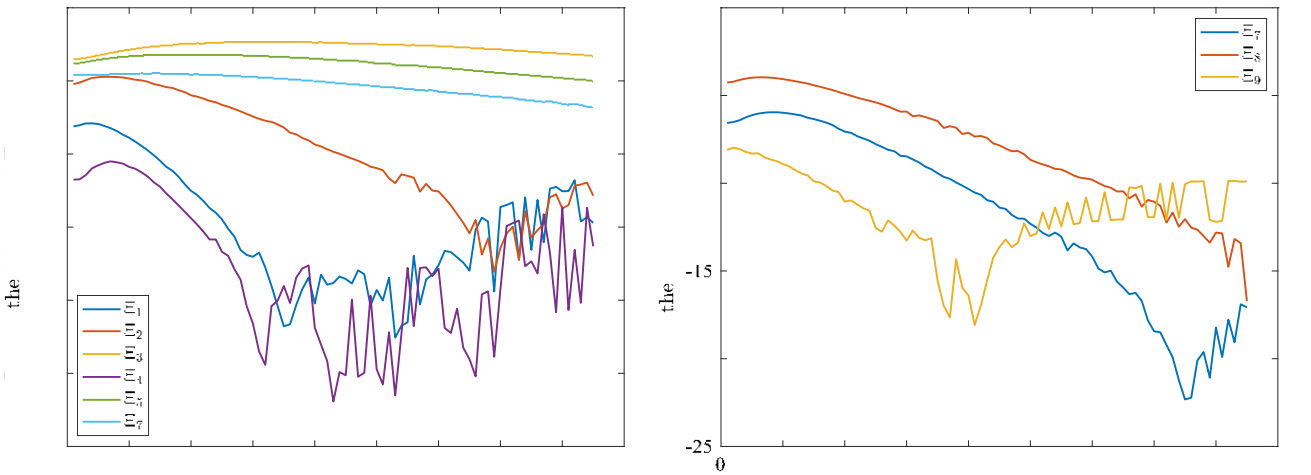

(b) Graphs of the log-likelihood functions for Ξ_i, $7 \leq i \leq 9$

Fig. 13 Graphs of the log-likelihood functions for the nine components of the latent Gaussian random field. Left and right panels are associated with the matrix-valued and scalar-valued Walpole's components, respectively

Fig. 14 CAD view of the apex geometry corresponding to the tip of the tank shown in the left panel in Fig. 1 (dashed lines show the region used for subsequent analysis), and boundary conditions used in the Laplace problem (see Sect. 3.1.1)

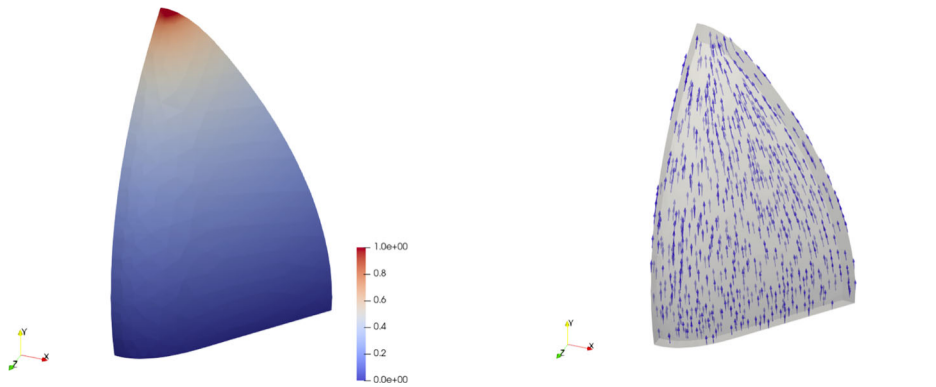

Fig. 15 CAD view of the apex geometry and boundary conditions used in the Laplace problem (see Sect. 3.1.1)

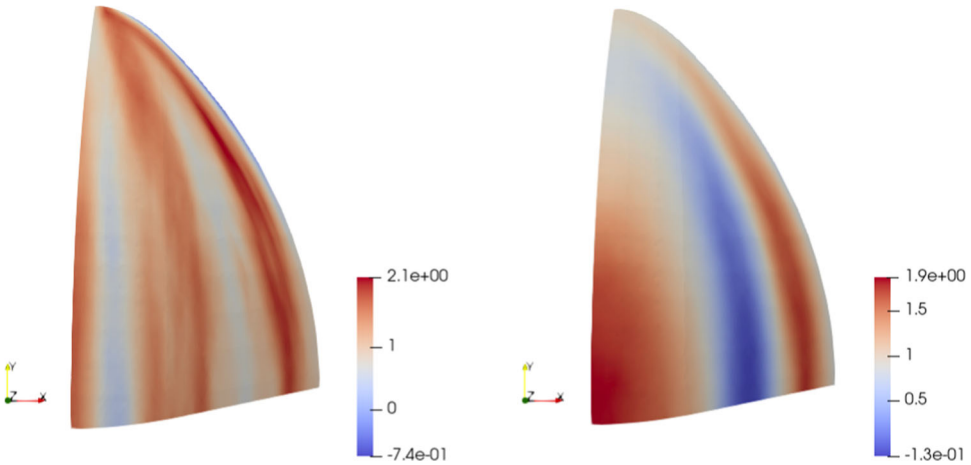

Fig. 16 Realizations of the latent Gaussian random field associated with the bulk modulus random field

(a) Scenario 1: $\boldsymbol{L} = (1, 1, 30)$ (b) Scenario 2: $\boldsymbol{L} = (30, 30, 30)$

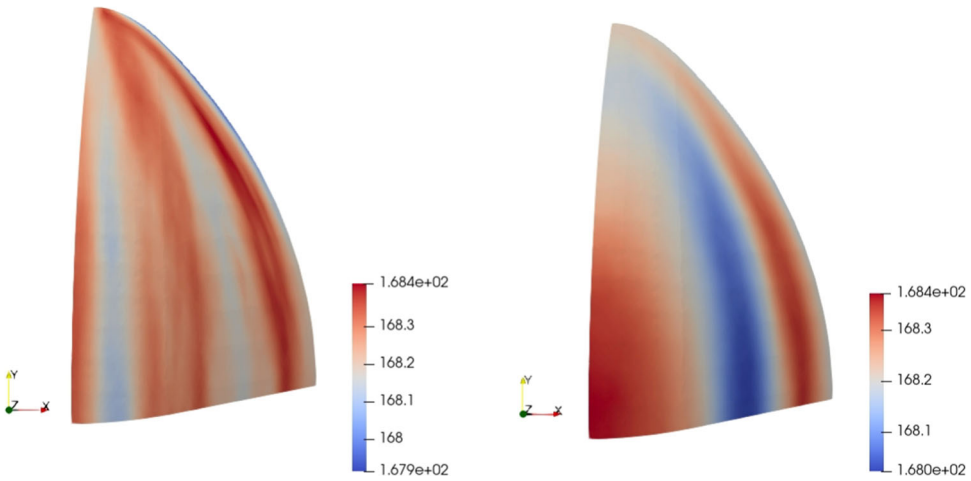

Fig. 17 Realizations of the non-Gaussian bulk modulus random field, in [GPa]

(a) Scenario 1: $\boldsymbol{L} = (1, 1, 30)$ (b) Scenario 2: $\boldsymbol{L} = (30, 30, 30)$

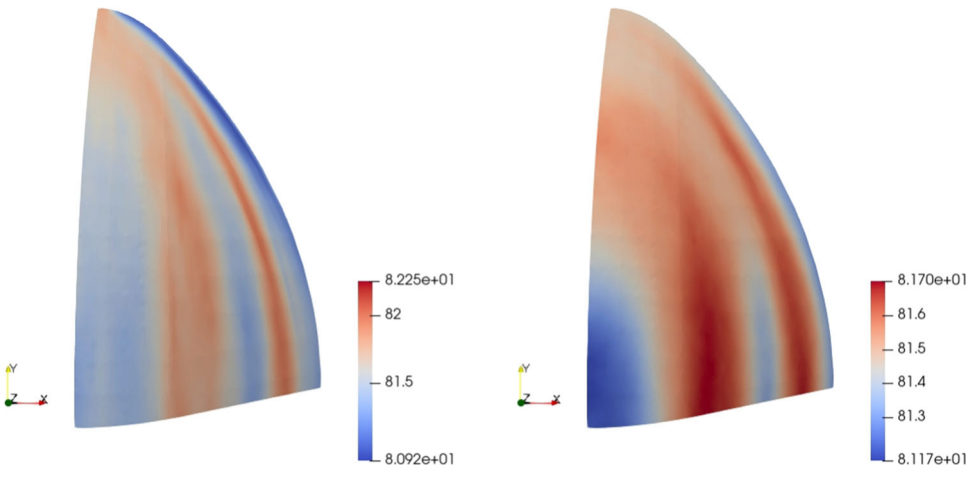

Fig. 18 Realizations of the non-Gaussian shear modulus random field, in [GPa]

(a) Scenario 1: $\boldsymbol{L} = (1, 1, 30)$ (b) Scenario 2: $\boldsymbol{L} = (30, 30, 30)$

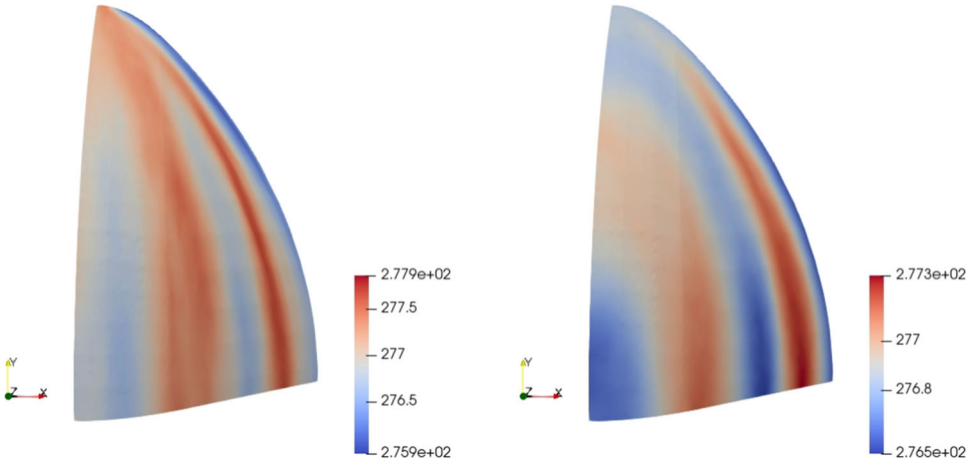

Fig. 19 Realizations of non-Gaussian random fields $\{C_{11}(\boldsymbol{x}), \boldsymbol{x} \in \mathcal{D}\}$ for the two scenarios

and $\boldsymbol{L}^{(k)} = (L_1^{(k)}, L_2^{(k)}, L_3^{(k)})^T$ is taken either as $\boldsymbol{L}^{(k)} = (1, 1, L_3^{(k)})$ (scenario 1) or as $\boldsymbol{L}^{(k)} = (L_3^{(k)}, L_3^{(k)}, L_3^{(k)})$ (scenario 2), where $\{L_3^{(k)}\}_{k=1}^9$ are given in Table 2. Realizations corresponding to these two cases are shown in Figs. 20 and 21.

Differences between all fields are very noticeable for and between each scenario, due to substantial variations in the correlation lengths (smaller correlation lengths implying higher-frequency oscillations along the associated direction; see Table 2). It is seen, for instance, that the latent field $\{\ _9(\boldsymbol{x}), \boldsymbol{x} \in \mathcal{D}\}$ exhibits more variations than the other two fields associated with the scalar components in the Walpole basis (namely, $\{\ _7(\boldsymbol{x}), \boldsymbol{x} \in \mathcal{D}\}$ and $\{\ _8(\boldsymbol{x}), \boldsymbol{x} \in \mathcal{D}\}$). The associated realizations for the components of the elasticity matrix are shown in Figs. 22 and 23.

5.3 Uncertainty propagation using the monte carlo approach

In this final section, we consider the propagation of material uncertainties on the quarter of the apex. We consider the stochastic linear elasticity problem with boundary conditions set to mimic inflation under inner pressure:

- Free-sliding Dirichlet boundary conditions are applied on the faces corresponding to $x = 0$, $y = 0$, and $z = 0$ (i.e., $u_x = 0$ on the face defined by $x = 0$, and similarly, $u_y = 0$ and $u_z = 0$ on faces where $y = 0$ and $z = 0$, respectively);
- An inflating pressure $p = 3$ [MPa] is applied on the inner surface of the apex: $(\boldsymbol{x})\boldsymbol{n}(\boldsymbol{x}) = -p\boldsymbol{n}(\boldsymbol{x})$, where is the stress tensor and $\boldsymbol{n}$ is the outward pointing normal unit vector at point $\boldsymbol{x}$ on the inner surface.

A Monte-Carlo approach is used as the stochastic solver, and the finite element method is deployed to solve for the displacement field for each realization of the stochastic fields. The mesh is comprised of 9,890 nodes and 41,232 P_1 finite elements (based on a convergence study), as shown in Fig. 24.

Figures 25 and 26 show the color contour of the displacement magnitude and Von Mises stress for the isotropic model, for $\boldsymbol{L} = (1, 1, 30)^T$ and $\boldsymbol{L} = (30, 30, 30)^T$ respectively. Similar results are displayed for the orthotropic model in Figs. 27 and 28.

Figure 29 shows the probability density functions of the maximum of displacement magnitude and Von Mises stress for the isotropic and orthotropic models, for both scenarios (estimated with 500 samples). These figures show that the selected quantities of interest are not very sensitive to correlation lengths (for a given symmetry class), but exhibit stronger dependence on the symmetry class—in terms of both mean and coefficient of variation. It is also confirmed that the isotropic model introduces less variability in the structural response. The corresponding mean value and the coefficients of variation for the maximum of displacement magnitude and Von Mises stress for each case are provided in Tables 3 and 4, respectively. In both cases, the structural response exhibits small variability, owing to the size of the domain over which homogenization is considered.

6 Conclusion

In this work, we considered the integration of spatially-dependent microstructure samples to model material symmetries in terms of both stochastic representation and impact on the structural response. These samples, obtained from experiments, correspond to EBSD measurements collected along a curvilinear path on a complex domain printed by power bed fusion. Using simple multiscale predictions, defined as the average of Voigt and Reuss bounds, we derived stochas-tic models for orthotropic elasticity random fields and for

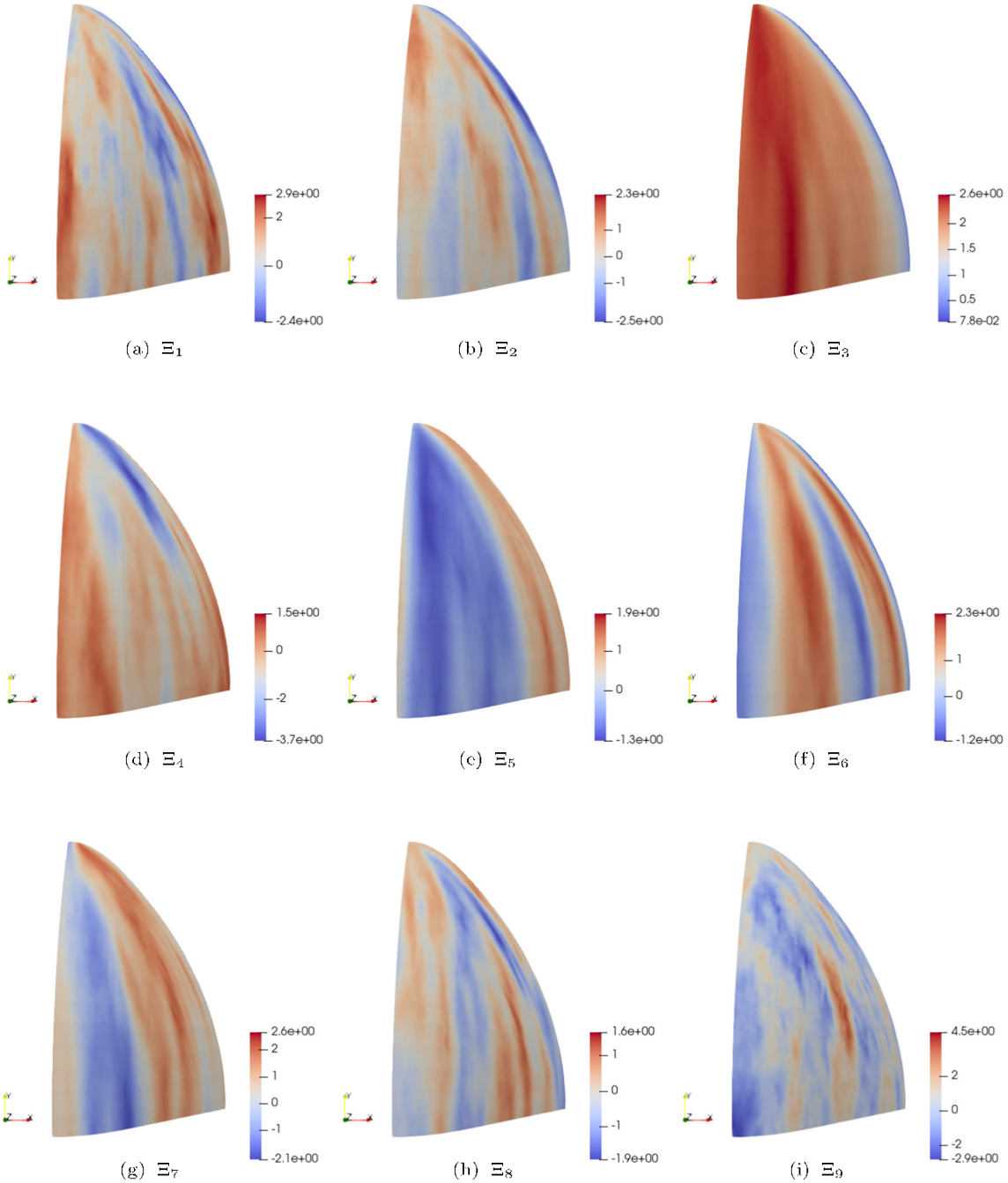

Fig. 20 Scenario 1: Realizations of the nine underlying Gaussian random fields

Table 2 Upper bounds for the correlation lengths in the orthotropic case

k	1	2	3	4	5	6	7	8	9
$L_3^{(k)}$ (mm)	8	12	64	14	36	28	18	14	4

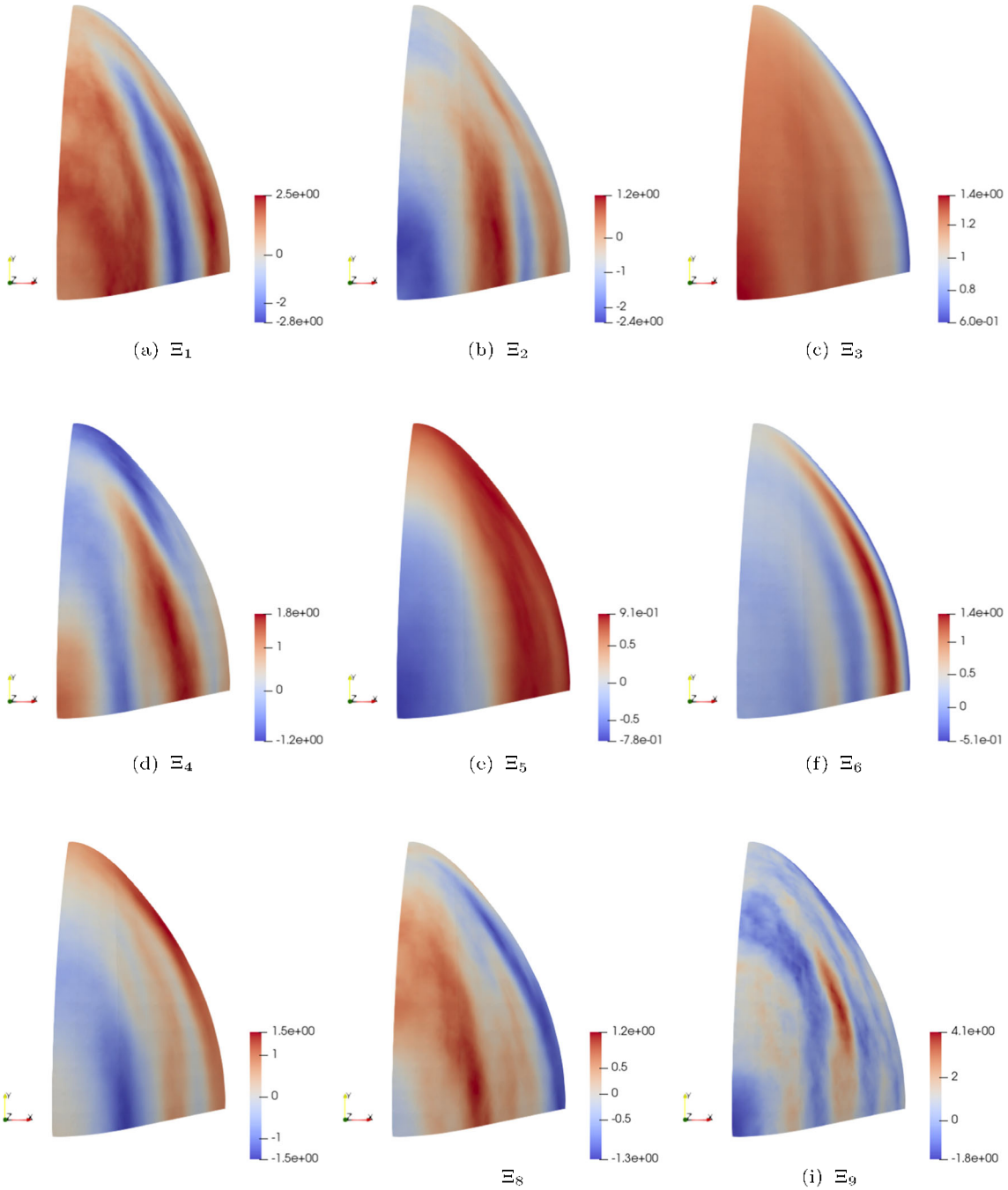

Fig. 21 Scenario 2: Realizations of the nine underlying Gaussian random fields

Table 3 Mean and coefficient of variation of the maximum of displacement magnitude for the isotropic and orthotropic cases, for both scenarios

Symmetry	Scenario	Mean (in [mm])	CV
Isotropic	1	0.0272	0.0020
	2	0.0272	0.0030
Orthotropic	1	0.0269	0.0057
	2	0.0269	0.0077

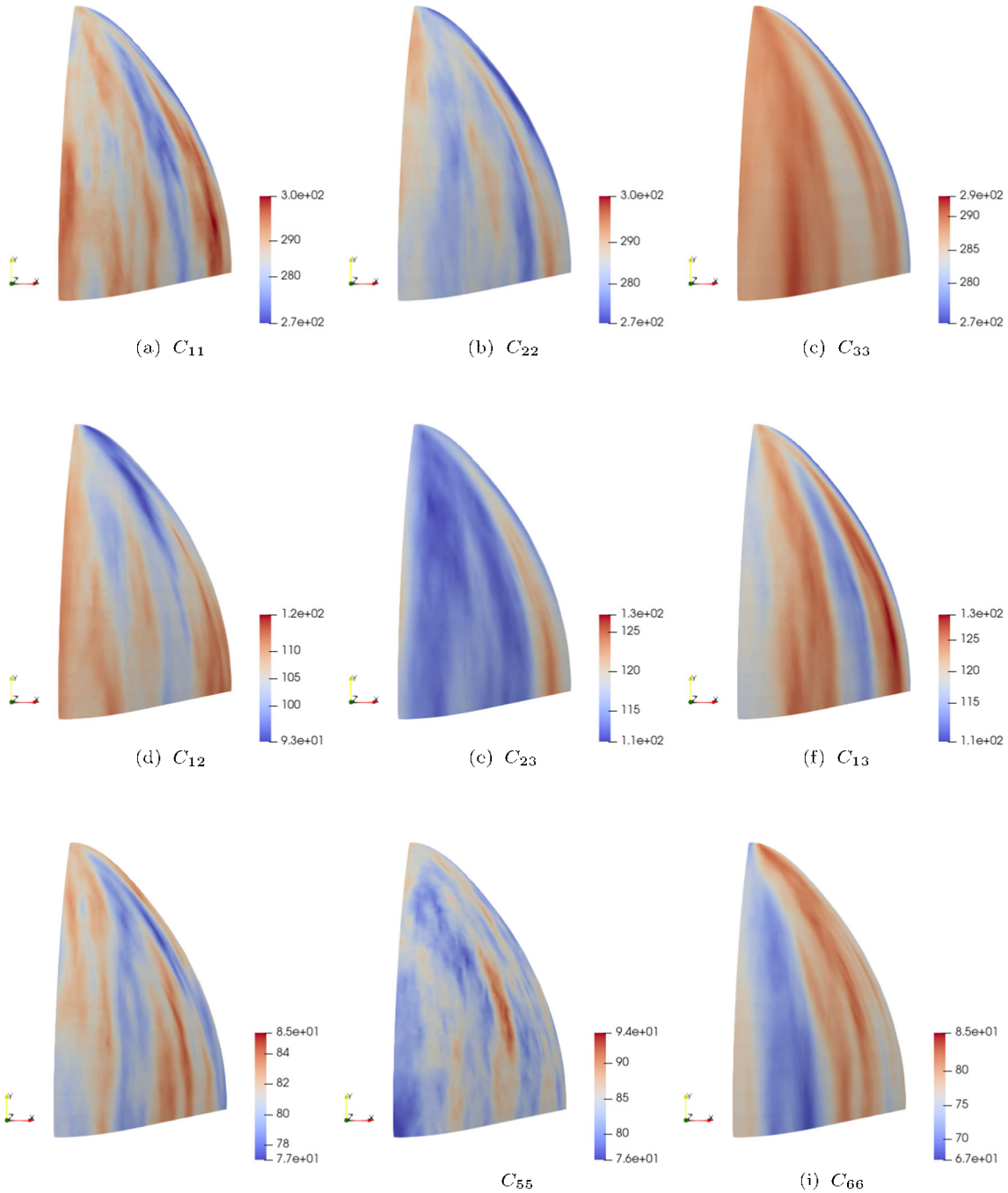

Fig. 22 Scenario 1: Realizations of the components of the elasticity matrix random field for the orthotropic case, in [GPa]

Table 4 Mean and coefficient of variation of the maximum of Von Mises stress for the isotropic and orthotropic cases with different correlation lengths

Symmetry		Mean (in [Pa])	CV
Isotropic	$(1, 1, 30)$	2.1774×10^8	0.0032
	$(30, 30, 30)$	2.1775×10^8	0.0026
Orthotropic	$(1, 1, L_i)$	2.1009×10^8	0.0191
	(L_i, L_i, L_i)	2.1014×10^8	0.0199

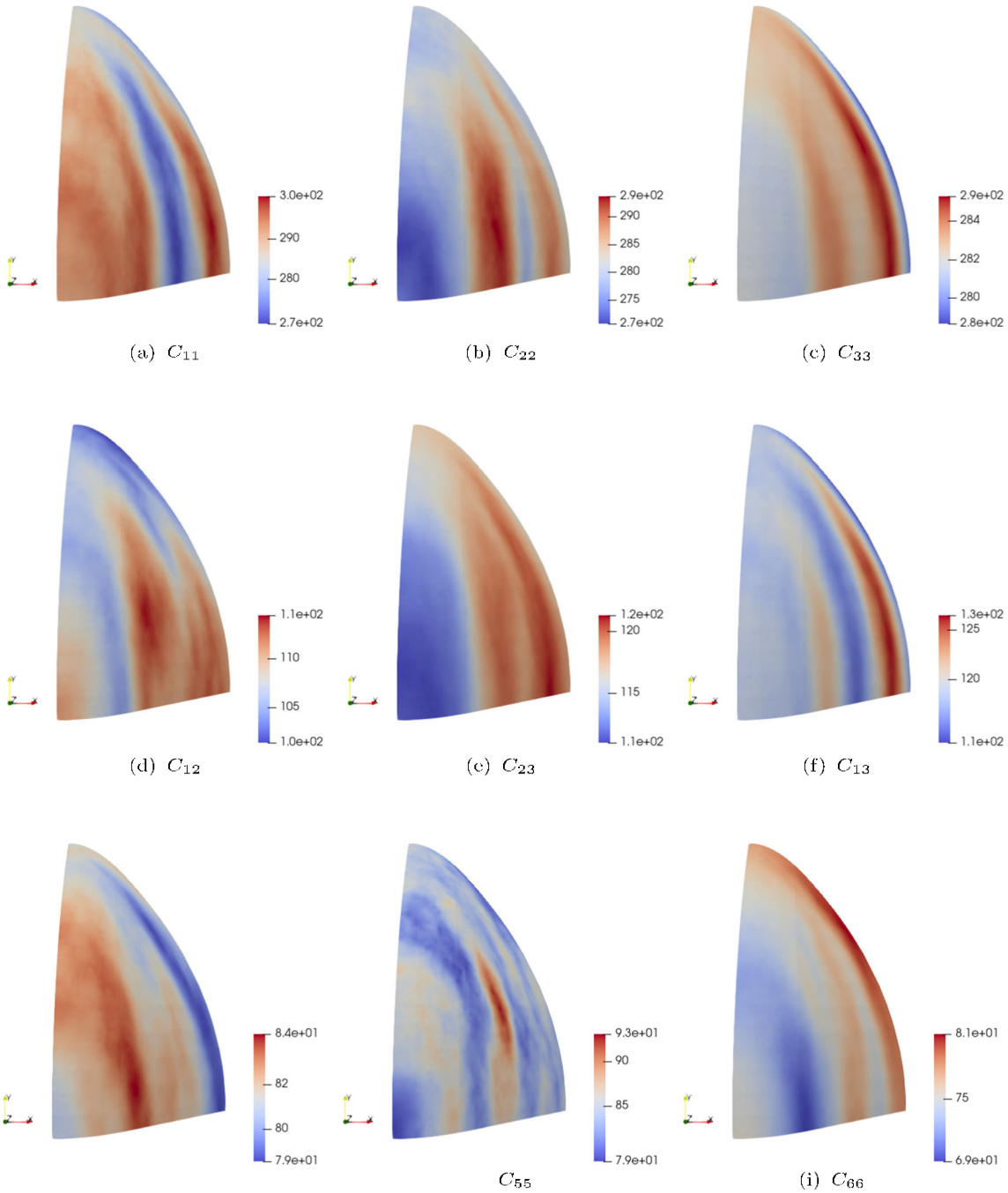

Fig. 23 Scenario 2: Realizations of the components of the elasticity matrix random field for the orthotropic case, in [GPa]

an isotropic approximation defined by projecting samples onto the set of isotropic tensors—using the Euclidean, Log-Riemannian, and Riemannian metrics. We showed that both models exhibit small statistical fluctuations, owing to the size of the microstructure, and that the isotropic approximation leads to an underestimation of the variations. We then proposed a methodology to infer spatial correlation lengths, using one single sample. Similar to calibration techniques in Gaussian process regression, the method involves pulling back samples from the non-Gaussian to the Gaussian space and applying a maximum likelihood estimator on conditional distributions. We finally performed uncertainty propagation on the apex domain, using the SPDE approach and the translation random field models. We showed that

Fig. 24 Finite element mesh for the apex subdomain

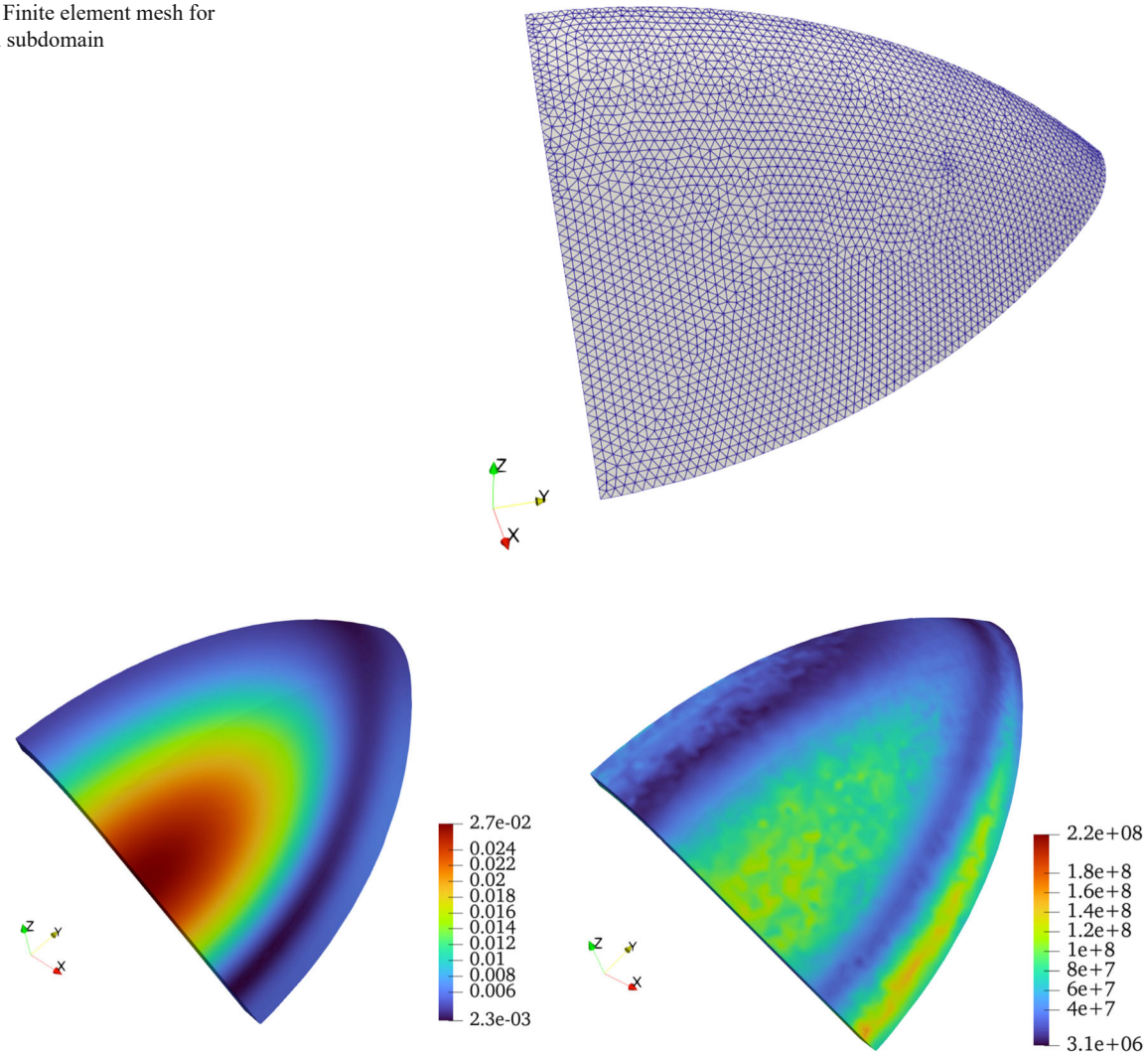

Fig. 25 Realizations of the displacement magnitude in [mm] and Von Mises stress in [Pa], for the isotropic case with $\boldsymbol{L} = (1, 1, 30)^T$ (scenario 1)

the selected quantities of interest, namely the maximum of displacement magnitude and maximum von Mises stress, exhibit small variability (as expected given the levels of fluctuation identified from multiscale results) and dependence on the symmetry class. They were, however, much less sensitive to the correlation lengths given the geometry and applied boundary conditions.

Acknowledgements The work of S.C. was supported by the National Science Foundation, Division of Civil, Mechanical and Manufacturing Innovation, under award CMMI-1942928. The work of J.G. was partially supported by the U.S. National Research Laboratory (US NRL) under contract N0017321P1059, as well as by the National Science Foundation, Division of Civil, Mechanical and Manufacturing Innovation, under award CMMI-1942928. The work of A.I., J.M., A.B., J.S., and C.S. was supported by the Office of Naval Research through U.S. Naval Research Laboratory's core funding. This support is gratefully acknowledged.

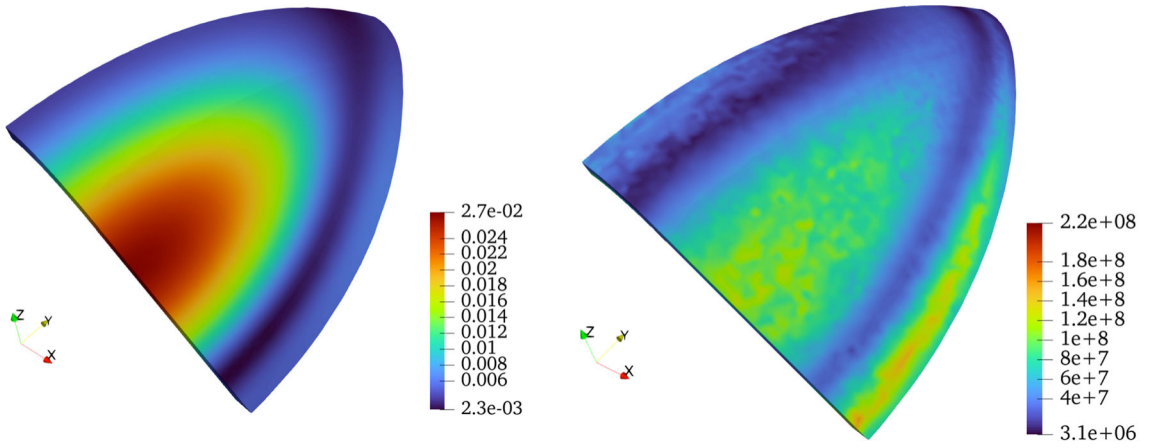

Fig. 26 Realizations of the displacement magnitude in [mm] and Von Mises stress in [Pa], for the isotropic case with $\boldsymbol{L} = (30, 30, 30)^T$ (scenario 2)

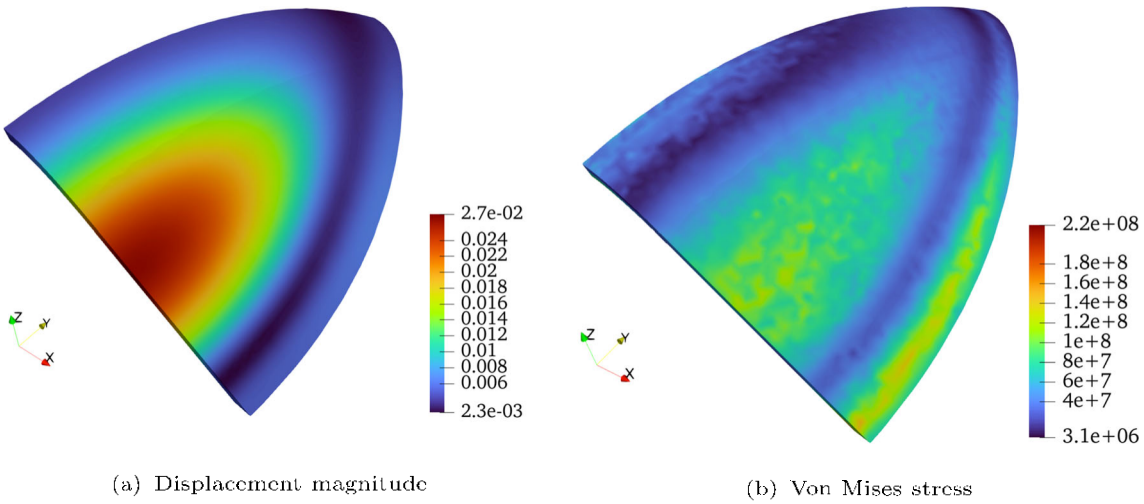

Fig. 27 Realizations of the displacement magnitude in [mm] and Von Mises stress in [Pa], for the orthotropic case and scenario 1

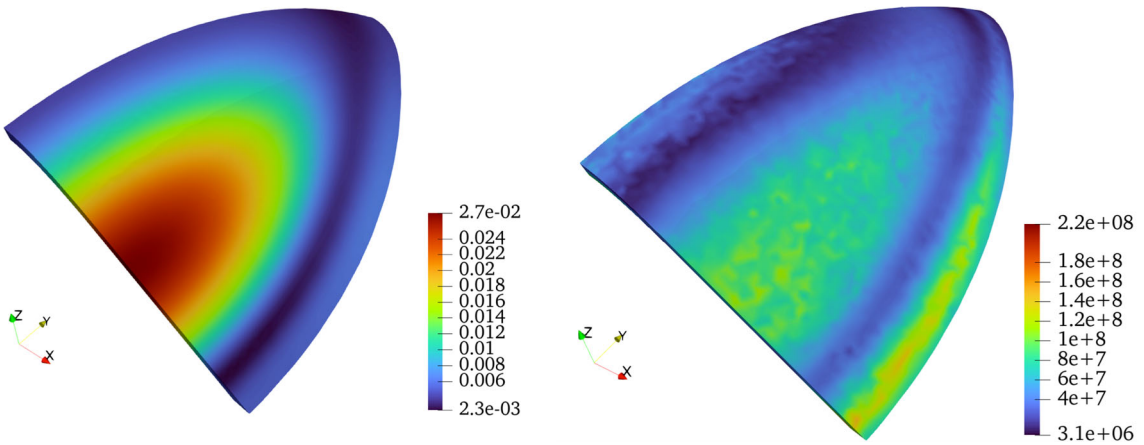

Fig. 28 Realizations of the displacement magnitude in [mm] and Von Mises stress in [Pa], for the orthotropic case and scenario 2

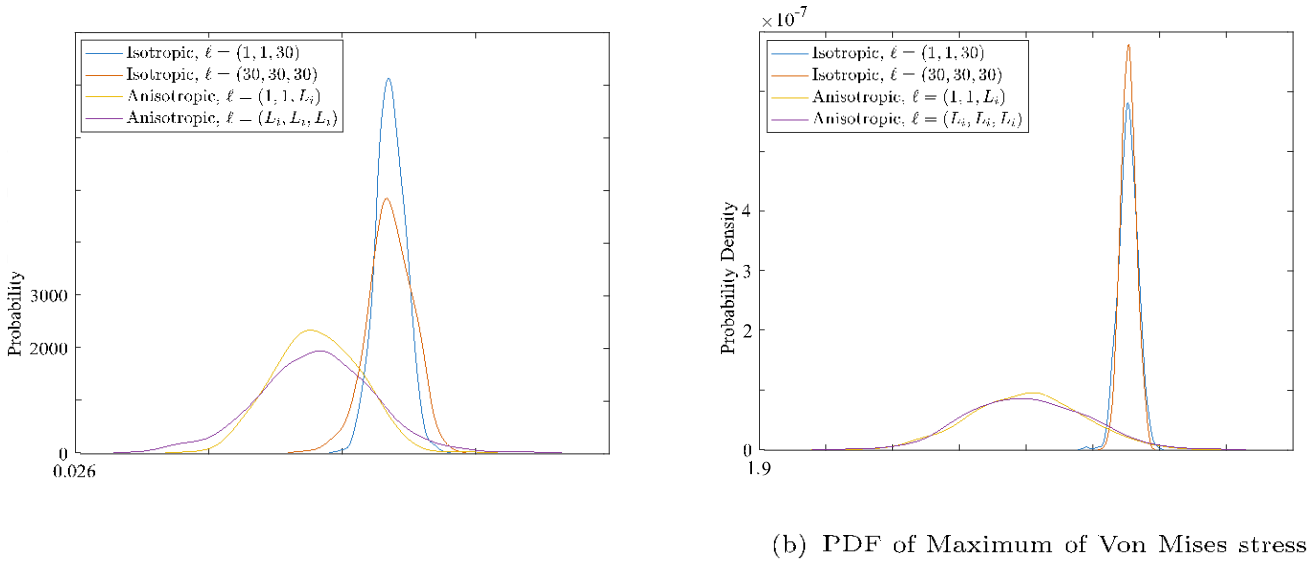

Fig. 29 Probability density functions of the maximum of displacement magnitude in [mm] and Von Mises stress in [Pa] for both isotropic and orthotropic cases with different correlation lengths, estimated with 500 samples

References

1. Alsalla HH, Smith C, Hao L (2018) Effect of build orientation on the surface quality, microstructure and mechanical properties of selective laser melting 316l stainless steel. Rapid Prototyp J 24(1):9–17
2. Mohammed HG, Ginta TL, Mustapha M (2021) The investigation of microstructure and mechanical properties of resistance spot welded AISI 316l austenitic stainless steel. Mater Today Proc 46:1640–1644
3. Yadroitsev I, Bertrand P, Smurov I (2007) Parametric analysis of the selective laser melting process. Appl Surf Sci 253(19):8064–8069
4. Sinha S, Szpunar JA, Kumar NK, Gurao N (2015) Tensile deformation of 316l austenitic stainless steel using in-situ electron backscatter diffraction and crystal plasticity simulations. Mater Sci Eng, A 637:48–55
5. Jayalakshmi M, Huilgol P, Bhat BR, Bhat KU (2016) Microstructural characterization of low temperature plasma-nitrided 316l stainless steel surface with prior severe shot peening. Mater Des 108:448–454
6. Rodrigues TA, Escobar J, Shen J, Duarte VR, Ribamar G, Avila JA, Maawad E, Schell N, Santos TG, Oliveira J (2021) Effect of heat treatments on 316 stainless steel parts fabricated by wire and arc additive manufacturing: Microstructure and synchrotron x-ray diffraction analysis. Addit Manuf 48:102428
7. Magarò P, Alaimo G, Carraturo M, Sgambitterra E, Maletta C (2023) A novel methodology for the prediction of the stress-strain response of laser powder bed fusion lattice structure based on a multi-scale approach. Mater Sci Eng, A 863:144526. https://doi.org/10.1016/j.msea.2022.144526
8. Hengsbach F, Koppa P, Holzweissig MJ, Aydinöz ME, Taube A, Hoyer K-P, Starykov O, Tonn B, Niendorf T, Tröster T et al (2018) Inline additively manufactured functionally graded multi-materials: microstructural and mechanical characterization of 316l parts with h13 layers. Progress Addit Manuf 3:221–231
9. Röttger A, Boes J, Theisen W, Thiele M, Esen C, Edelmann A, Hellmann R (2020) Microstructure and mechanical properties of 316l austenitic stainless steel processed by different SLM devices. Int J Adv Manuf Technol 108:769–783
10. Jiang D, Ning F (2022) Anisotropic deformation of 316l stainless steel overhang structures built by material extrusion based additive manufacturing. Addit Manuf 50:102545
11. Riemer A, Leuders S, Thöne M, Richard H, Tröster T, Niendorf T (2014) On the fatigue crack growth behavior in 316l stainless steel manufactured by selective laser melting. Eng Fract Mech 120:15–25
12. Liverani E, Toschi S, Ceschini L, Fortunato A (2017) Effect of selective laser melting (SLM) process parameters on microstructure and mechanical properties of 316l austenitic stainless steel. J Mater Process Technol 249:255–263
13. Kamariah M, Harun W, Khalil N, Ahmad F, Ismail M, Sharif S (2017) Effect of heat treatment on mechanical properties and microstructure of selective laser melting 316l stainless steel. In: IOP conference series: materials science and engineering, vol. 257, p 012021. IOP Publishing
14. Iliopoulos A, Thomas J, Steuben J, Saunders R, Michopoulos J, Bagchi A, Birnbaum A (2020) Statistical analysis of tensile tests performed on 316l specimens manufactured by directed energy deposition. In: International design engineering technical conferences and computers and information in engineering conference, vol 83983, pp 009–09024. American Society of Mechanical Engineers
15. Güden M, Yavas H, Tanrikulu AA, Tasdemirci A, Akin B, Enser S, Karakus A, Hamat BA (2021) Orientation dependent tensile properties of a selective-laser-melt 316l stainless steel. Mater Sci Eng, A 824:141808. https://doi.org/10.1016/j.msea.2021.141808
16. Mahadevan S, Nath P, Hu Z (2021) Uncertainty quantification for additive manufacturing process improvement: recent advances. ASCE-ASME J Risk Uncert Engrg Sys Part B Mech Engrg 8(1)
17. Maleki E, Bagherifard S, Sabouri F, Guagliano M (2021) Effects of hybrid post-treatments on fatigue behaviour of notched LPBF alsi10mg: Experimental and deep learning approaches. Proc Struct Integr 34:141–153
18. Ren K, Chew Y, Liu N, Zhang Y, Fuh J, Bi G (2021) Integrated numerical modelling and deep learning for multi-layer cube deposition planning in laser aided additive manufacturing. Virtual Phys Prototyp 16(3):318–332

19. Mamedipaka R, Thapliyal S (2023) Data-driven model for predicting tensile properties of wire arc additive manufactured 316l steels and its validation. J Mater Eng Perform, pp 1–9
20. Maloth T, Ozturk D, Hommer GM, Pilchak AL, Stebner AP, Ghosh S (2020) Multiscale modeling of cruciform dwell tests with the uncertainty-quantified parametrically homogenized constitutive model. Acta Mater 200:893–907
21. Kotha S, Ozturk D, Smarslok B, Ghosh S (2020) Uncertainty quantified parametrically homogenized constitutive models for microstructure-integrated structural simulations. Integrat Mater Manufact Innov 9(4):322–338
22. Ozturk D, Kotha S, Ghosh S (2021) An uncertainty quantification framework for multiscale parametrically homogenized constitutive models (PHCMS) of polycrystalline ti alloys. J Mech Phys Solids 148:104294
23. Weber G, Pinz M, Ghosh S (2022) Machine learning-enabled self-consistent parametrically-upscaled crystal plasticity model for ni-based superalloys. Comput Methods Appl Mech Eng 115384
24. Pinz M, Storck S, Montalbano T, Croom B, Salahudin N, Trexler M, Ghosh S (2022) Efficient computational framework for image-based micromechanical analysis of additively manufactured TI-6AL-4V alloy. Addit Manuf 60:103269
25. Senthilnathan A, Javaheri I, Sundararaghavan V, Acar P (2023) Computational characterization and model verification for 3d microstructure reconstruction of additively manufactured materials. In: AIAA SCITECH 2023 forum
26. Korshunova N, Alaimo G, Hosseini SB, Carraturo M, Reali A, Niiranen J, Auricchio F, Rank E, Kollmannsberger S (2021) Image-based numerical characterization and experimental validation of tensile behavior of octet-truss lattice structures. Addit Manufact 41:101949. https://doi.org/10.1016/j.addma.2021.101949
27. Zhao K, Wang B, Xue H, Wang Z (2022) Effect of material inhomogeneity on the crack tip mechanical field and SCC growth rate of 52m/316l dissimilar metal welded joints. Metals 12(10):1683
28. Benito S, Egels G, Hartmaier A, Weber S (2023) Statistical characterization of segregation-driven inhomogeneities in metallic microstructures employing fast first-order variograms. Mater Today Commun 34:105016
29. Chu S, Guilleminot J, Kelly C, Abar B, Gall K (2021) Stochastic modeling and identification of material parameters on structures produced by additive manufacturing. Comput Methods Appl Mech Eng 387:114166
30. Ghanem R, Higdon D, Owhadi H (2017) Handbook of uncertainty quantification. Springer
31. Le Maître O, Knio O (2010) Spectral methods for uncertainty quantification: with applications to computational fluid dynamics. Springer
32. Andreau O, Koutiri I, Peyre P, Penot J-D, Saintier N, Pessard E, De Terris T, Dupuy C, Baudin T (2019) Texture control of 316l parts by modulation of the melt pool morphology in selective laser melting. J Mater Process Technol 264:21–31. https://doi.org/10.1016/j.jmatprotec.2018.08.049
33. Iliopoulos A, Michopoulos JG, Birnbaum A, Steuben JC, Stew-art C, Rowenhorst D (2020) Structural performance modeling of additively manufactured parts under process-induced inhomogeneity and property anisotropy. ASTM ICAM virtual conference
34. Ledbetter HM (1981) Elastic constants of polycrystalline copper at low temperatures. Relationship to single-crystal elastic constants. Physica Status Solid 66(2):477–484
35. Ostoja-Starzewski M (2008) Microstructural randomness and scaling in mechanics of materials. Chapman and Hall/CRC/Taylor and Francis
36. Villalobos-Portillo EE, Fuentes-Montero L, Montero-Cabrera ME, Burciaga-Valencia DC, Fuentes-Cobas LE (2019) Polycrystal piezoelectricity: revisiting the Voigt–Reuss–Hill approximation. Mater Res Express 6(11):115705. https://doi.org/10.1088/2053-1591/ab46f2
37. Norris AN (2006) Elastic moduli approximation of higher symmetry for the acoustical properties of an anisotropic material. J Acoust Soc Am 119(4):2114–2121
38. Arsigny V, Fillard P, Pennec X, Ayache N (2006) Log-euclidean metrics for fast and simple calculus on diffusion tensors. Magn Reson Med 56:411–421
39. Moakher M, Norris AN (2006) The closest elastic tensor of arbitrary symmetry to an elasticity tensor of lower symmetry. J Elast 85:215–263
40. Soize C (2006) Non-Gaussian positive-definite matrix-valued random fields for elliptic stochastic partial differential operators. Comput Methods Appl Mech Eng 195(1):26–64. https://doi.org/10.1016/j.cma.2004.12.014
41. Staber B, Guilleminot J (2017) Stochastic modeling and generation of random fields of elasticity tensors: a unified information-theoretic approach. Comptes Rendus Mécanique 345(6):399–416. https://doi.org/10.1016/j.crme.2017.05.001
42. Guilleminot J (2020) 12–modeling non-Gaussian random fields of material properties in multiscale mechanics of materials. In: Wang Y, McDowell DL (eds) Uncertainty quantification in multiscale materials modeling. Elsevier Series in Mechanics of Advanced Materials, pp 385–420. Woodhead Publishing
43. Das S, Ghanem R (2009) A bounded random matrix approach for stochastic upscaling. Multiscale Model Simul 8(1):296–325
44. Guilleminot J, Soize C (2013) On the statistical dependence for the components of random elasticity tensors exhibiting material symmetry properties. J Elast 111(2):109–130. https://doi.org/10.1007/s10659-012-9396-z
45. Guilleminot J, Soize C (2013) Stochastic model and generator for random fields with symmetry properties: application to the mesoscopic modeling of elastic random media. Multiscale Model Simul 11(3):840–870
46. Guilleminot J, Soize C (2014) Itô SDE-based generator for a class of non-Gaussian vector-valued random fields in uncertainty quantification. SIAM J Sci Comput 36(6):2763–2786
47. Baxter SC, Acton KA (2019) Simulations of non-Gaussian property fields based on the apparent properties of statistical volume elements. ASCE-ASME J Risk Uncert Engrg Sys Part B Mech Engrg 5(3):030906
48. Grigoriu M (2016) Microstructure models and material response by extreme value theory. SIAM/ASA J Uncertain Quantif 4(1):190–217
49. Shivanand SK, Rosić B, Matthies HG (2021) Stochastic modelling of symmetric positive-definite material tensors
50. Malyarenko A, Ostoja-Starzewski M (2017) A random field formulation of Hooke's law in all elasticity classes. J Elast 127(2):269–302. https://doi.org/10.1007/s10659-016-9613-2
51. Malyarenko A, Ostoja-Starzewski M (2020) Tensor random fields in continuum mechanics, pp 2433–2441. Springer, Berlin
52. Malyarenko A, Ostoja-Starzewski M (2016) Spectral expansion of three-dimensional elasticity tensor random fields. In: Silvestrov S, Rančić M (eds) Engineering mathematics I. Springer, Cham, pp 281–300
53. Malyarenko A, Ostoja-Starzewski M (2023) Tensor- and spinor-valued random fields with applications to continuum physics and cosmology. Probab Surv 20:1–86
54. Walpole L (1984) Fourth-rank tensors on the thirty-two crystal classes: multiplication tables. Proc R Soc Lond A 391:149–179. https://doi.org/10.1098/rspa.1984.0008
55. Grigoriu M (1984) Crossings of non-gaussian translation processes. J Eng Mech 110(4):610–620
56. Lindgren F, Rue H, Lindström J (2011) An explicit link between gaussian fields and gaussian markov random fields: the stochastic

partial differential equation approach. J R Stat Soc Ser B 73(4):423–498. https://doi.org/10.1111/j.1467-9868.2011.00777.x
57. Lindgren F, Bolin D, Rue H (2022) The SPDE approach for gaussian and non-gaussian fields: 10 years and still running. Spatial Stat 50:100599. https://doi.org/10.1016/j.spasta.2022.100599
58. Whittle P (1954) On stationary processes in the plane. Biometrika 41(3–4):434–449. https://doi.org/10.1093/biomet/41.3-4.434
59. Whittle P (1963) Stochastic processes in several dimensions. Bull Int Stat Inst 40:974–994
60. Fuglstad G-A, Lindgren F, Simpson D, Rue H (2015) Exploring a new class of nonstationary spatial Gaussian random fields with varying local anisotropy. Stat Sin 25(1):115–133. https://doi.org/10.5705/ss.2013.106w
61. Roininen L, Huttunen JMJ, Lasanen S (2014) Whittle-Matérn priors for bayesian statistical inversion with applications in electrical impedance tomography. Inverse Probl Imaging 8(2):561–586. https://doi.org/10.3934/ipi.2014.8.561
62. Dunlop MM, Stuart AM (2016) The Bayesian formulation of EIT: analysis and algorithms. Inverse Probl Imaging 10(4):1007–1036. https://doi.org/10.3934/ipi.2016030
63. Sidén P, Eklund A, Bolin D, Villani M (2017) Fast Bayesian whole-brain FMRI analysis with spatial 3d priors. NeuroImage 146:211–225. https://doi.org/10.1016/j.neuroimage.2016.11.040
64. Roininen L, Girolami M, Lasanen S, Markkanen M (2019) Hyperpriors for Matérn fields with applications in Bayesian inversion. Inverse Probl Imaging 13(1):1–29. https://doi.org/10.3934/ipi.2019001
65. Sidén P, Lindgren F, Bolin D, Eklund A, Villani M (2019) Spatial 3d Matérn priors for fast whole-brain FMRI analysis. arXiv:1906.10591
66. Mejia AF, Yue YR, Bolin D, Lindgren F, Lindquist MA (2020) A Bayesian general linear modeling approach to cortical surface FMRI data analysis. J Am Stat Assoc 115(530):501–520. https://doi.org/10.1080/01621459.2019.1611582
67. Bolin D, Lindgren F (2011) Spatial models generated by nested stochastic partial differential equations, with an application to global ozone mapping. Ann Appl Stat 5(1):523–550. https://doi.org/10.1214/10-AOAS383
68. Guilleminot J, Asadpoure A, Tootkaboni M (2019) Topology optimization under topologically dependent material uncertainties. Struct Multidiscip Optim 60:1283–1287. https://doi.org/10.1007/s00158-019-02247-1
69. Staber B, Guilleminot J (2018) A random field model for anisotropic strain energy functions and its application for uncertainty quantification in vascular mechanics. Computer Methods Appl Mech Eng 333:94–113. https://doi.org/10.1016/j.cma.2018.01.001
70. Chu S, Guilleminot J (2019) Stochastic multiscale modeling with random fields of material properties defined on nonconvex domains. Mech Res Commun 97:39–45
71. Bolin D, Kirchner K (2020) The rational SPDE approach for Gaussian random fields with general smoothness. J Comput Graph Stat 29(2):274–285. https://doi.org/10.1080/10618600.2019.1665537
72. Bolin D, Wallin J (2020) Multivariate type g Matérn stochastic partial differential equation random fields. J R Stat Soc Ser B Stat Methodol 82(1):215–239. https://doi.org/10.1111/rssb.12351
73. Daon Y, Stadler G (2018) Mitigating the influence of the boundary on PDE-based covariance operators. Inverse Probl Imaging 12(5):1083–1102. https://doi.org/10.3934/ipi.2018045
74. Khristenko U, Scarabosio L, Swierczynski P, Ullmann E, Wohlmuth B (2019) Analysis of boundary effects on PDE-based sampling of Whittle-Matérn random fields. SIAM/ASA J Uncert Quant 7(3):948–974. https://doi.org/10.1137/18M1215700
75. Jaynes E (1957) Information theory and statistical mechanics i. Phys Rev 106(4):620–630. https://doi.org/10.1103/PhysRev.106.620
76. Jaynes E (1957) Information theory and stastitical mechanics ii. Phys Rev 108(2):171–190. https://doi.org/10.1103/PhysRev.108.171
77. Hun D-A, Guilleminot J, Yvonnet J, Bornert M (2019) Stochastic multiscale modeling of crack propagation in random heterogeneous media. Int J Numer Meth Eng 119(13):1325–1344
78. Soize C (2000) A nonparametric model of random uncertainties for reduced matrix models in structural dynamics. Probab Eng Mech 15(3):277–294
79. Tran V, Guilleminot J, Brisard S, Sab K (2016) Stochastic modeling of mesoscopic elasticity random field. Mech Mater 93:1–12. https://doi.org/10.1016/j.mechmat.2015.10.007